Scaling behaviour of magnetization for temperatures in the vicinity of, and far from, the ferromagnetic–paramagnetic phase transition in amorphous $Fe_{90-x}Co_xZr_{10}$ and $Fe_{90+y}Zr_{10-y}$ alloys

P D Babu† and S N Kaul‡

School of Physics, University of Hyderabad, Central University PO, Hyderabad 500 046, Andhra Pradesh, India

Abstract. Asymptotic critical exponents and amplitudes as well as the leading 'correction-to-scaling' (CTS) amplitudes have been accurately determined through an elaborate analysis of magnetization data taken on amorphous $Fe_{90-x}Co_xZr_{10}(0 \leqslant x \leqslant 6)$ and $Fe_{90+y}Zr_{10-y}(y = 0, 1)$ alloys in the critical region. Consistent with the Harris criterion, asymptotic critical exponents and the universal amplitude ratio Dm_0^δ/h_0 do not depend on composition and possess values the same as those predicted by theory for an ordered spin system with $n = d = 3$. The leading amplitude ratio $a_{M1}^-/a_{\chi1}^+$, which is *characteristic* of ferromagnets with quenched random disorder and for which no theoretical estimate is presently available, is *composition independent* and probably universal. The fraction of spins actually participating in the ferromagnetic (FM)–paramagnetic (PM) transition occurring at $T = T_C$ is small and increases with Co substitution. While the magnetic equation of state (MES) in linear scaling variables and its counterpart in nonlinear scaling variables, valid for a second-order phase transition, form *equivalent* descriptions of magnetization, $M(T, H)$, data in the asymptotic critical region (ACR), the latter version of MES alone reproduces closely the observed $M(T, H)$ behaviour in a temperature range as wide as $0.45T_C \lesssim T \lesssim 1.5T_C$. Nonanalytic CTS terms dominate over analytic ones in the ACR but the reverse is true for temperatures outside the ACR. Initial susceptibility follows the generalized Curie–Weiss law from T_C to $\simeq 1.5T_C$ and thereby permits an accurate determination of atomic moment in the PM state. The results of the present investigation provide strong experimental evidence for weak itinerant ferromagnetism in the glassy alloys in question.

1. Introduction

Static critical behaviour near the ferromagnetic–paramagnetic (FM–PM) phase transition of amorphous (a-) $Fe_{90+y}Zr_{10-y}(0 \leqslant y \leqslant 2)$ alloys has been investigated using the various experimental techniques such as bulk magnetization (BM) [1–5], ac susceptibility (ACS) [6, 7], ferromagnetic resonance (FMR) [8, 9], electrical resistivity (ρ) [10, 11] and small-angle neutron scattering (SANS) [12] during the past decade and yet the nature of the FM–PM transition at T_C (the Curie point) and the type of magnetic ordering for $T < T_C$ has eluded a complete understanding so far. Early BM and $\rho(T)$ data [2, 3, 10] taken on a-$Fe_{90-x}(Ni, Co)_xZr_{10}$ and a-$Fe_{90+y}Zr_{10-y}$ alloys over a wide range of temperatures

† Present address: Inter-university Consortium for DAE Facilities, Bombay Centre, Bhabha Atomic Research Centre, Trombay, Bombay 400 085, India.
‡ Author to whom correspondence should be addressed.

around T_C yielded values for the critical exponents α, β and γ for zero-field specific heat, spontaneous magnetization, $M_S(T) \equiv M(T, H = 0)$, and initial susceptibility, $\chi_0(T)$, that are in complete disagreement with the predictions of the renormalization group (RG) calculations [13–18], as explained below. In conformity with the heuristic arguments due to Harris [19] (the famous Harris criterion), the RG theories [13–18], based on the random-exchange (RE) model (which combines within itself both quenched random site- and bond-diluted spin models), predict that the critical behaviour of quenched random spin systems with space dimensionality d depends on the *sign* of the specific heat critical exponent α_p of the pure (ordered) system. If $\alpha_p < 0$ (i.e., for $d = 3$ Heisenberg and $d = 3$ XY systems with spin dimensionality $n = 3$ and $n = 2$, respectively), quenched randomness acts as an irrelevant scaling field and hence leaves the sharpness of the transition as well as the values of the static critical exponents of the pure system *unaltered*. If $\alpha_p > 0$ (i.e., for a $d = 3$ Ising system with $n = 1$), a *crossover* from pure to *random* fixed point (which is characterized by critical exponents whose values are widely different from the pure ones, so much so that the exponent α changes sign, i.e., $\alpha_r < 0$) occurs. Going by past experience that the asymptotic critical behaviour of several 3D transition metal–metalloid amorphous alloys is adequately described [20–23] by the random exchange Heisenberg model (REHM), the alloys in question are also expected to follow the same trend. Contrary to this expectation, the values of the exponents β and $\gamma(\alpha)$ for the glassy alloys $Fe_{90-x}(Ni, Co)_x Zr_{10}$ and $Fe_{90+y}Zr_{10-y}$, deduced [2, 3, 10] from early BM ($\rho(T)$) data, are roughly 1.4 (10) *times larger* than the RG estimates [18] for an isotropic nearest-neighbour (NN) $d = 3$ Heisenberg ferromagnet. Such unphysically large exponent values were taken to reflect a large fluctuation in the exchange interaction. This inference combined with the SANS result [12] that the spin–spin correlation length does not diverge at T_C led some workers [12, 24] to conclude that the long-range ferromagnetic ordering of the conventional type does not develop in these alloys at any temperature. However, it was later demonstrated that these anomalously large exponent values result from a major flaw in the previous data analysis and that early BM data [2], when analysed properly [4], yield values for the exponents β and γ that are fairly close to those theoretically predicted for a $d = n = 3$ spin system. The results of this reanalysis were subsequently confirmed by other investigations [5–9] involving BM, ACS and FMR measurements on glassy alloys with the same or similar nominal composition. Though these refinements narrow down the spread in the exponent values from about 40 to 10%, the theoretical estimates [13, 14, 16, 18] for the critical exponents that characterize $d = 3$ quenched random-exchange Heisenberg ($n = 3$) and Ising ($n = 1$) fixed points fall well within this 10% range [8]. Therefore, even the most refined results reported until now remain inconclusive so far as the exact nature of the FM–PM transition is concerned. The situation is further complicated by the observation, based on the recent ac susceptibility data [7], that the effective Kouvel–Fisher [25] susceptibility exponent $\gamma^*(T)$ attains the isotropic $d = 3$ Heisenberg value near $\epsilon = (T - T_C)/T_C \approx 10^{-2}$ but, as T_C is approached closer than $\epsilon = 10^{-2}$, $\gamma^*(T)$ falls to as low a value as 1.1 at $\epsilon \approx 5 \times 10^{-3}$. Such a steep fall in the value of $\gamma^*(T)$ has been attributed [7] to the effect of anisotropy, which, most probably, has its origin in spin–orbit coupling.

A close scrutiny of the results published so far reveals that most of the measurements have been performed in a temperature range which either completely or partly lies outside the asymptotic critical region (ACR $= |\epsilon| \lesssim 10^{-2}$). The values for the critical exponents obtained in this temperature range are, therefore, not the true asymptotic values which the theory predicts. Even in those cases where T_C was approached closer than $\epsilon = 10^{-2}$, data have been fitted to a *single power law* over a wide range of temperatures in the vicinity of T_C and such a data analysis invariably yields an *effective* critical exponent whose value

depends on the temperature range chosen for the fit. Thus, no definite conclusions regarding the nature of the leading singularity at T_C can be drawn from a quantitative comparison between the values of *effective* critical exponents reported in the literature and those of the *asymptotic* critical exponents yielded by the theory. Alternatively, the universality class to which a-$Fe_{90-x}Co_xZr_{10}$ and a-$Fe_{90+y}Zr_{10-y}$ alloys belong can be unambiguously established only when the true asymptotic values of the critical exponents are determined experimentally and the values so obtained compared with the theoretical predictions. With this aim in mind, values of asymptotic (leading correction-to-scaling (CTS)), critical exponents β and γ and critical amplitudes (amplitudes) have been accurately determined from high-precision BM measurements made on a-$Fe_{90-x}Co_xZr_{10}(0 \leqslant x \leqslant 6)$ and a-$Fe_{90+y}Zr_{10-y}(y = 0, 1)$ alloys in the asymptotic critical region through an elaborate data analysis. Results of various methods of analysis have been compared so as to clearly distinguish between effective and asymptotic critical exponents and amplitudes. Moreover, this comparison helps in identifying the main source of the spread in the previously reported exponent values. Another important aspect of the present work is the result that magnetization satisfies the generalized magnetic equation of state in nonlinear scaling variables over a temperature range as wide as $0.4T_C \lesssim T \lesssim 1.5T_C$.

2. Experimental details

Amorphous (a-) $Fe_{90-x}Co_xZr_{10}(x = 0, 1, 2, 4, 6)$ and $Fe_{90+y}Zr_{10-y}(y = 0, 1)$ alloys were prepared under inert (high-purity argon) atmosphere by single-roller melt-quenching technique in the form of long ribbons of $\sim$ 1–2 mm width and 30–40 μm thickness. The amorphous nature of the ribbons so prepared was verified by the x-ray diffraction method using Mo Kα radiation and later confirmed by high-resolution electron microscopic examination. A detailed compositional analysis [20] revealed no deviation from the nominal composition within the resolution limit of 0.01 at.% (Fe or Co) over the length ($\simeq$ 20 cm) of the alloy ribbons. In view of the observed composition dependence of T_C, the fact that concentration fluctuations, if present, do not exceed 0.01 at.% places an *upper bound* on the spread in T_C as $\delta T_C = 0.1$ K. For this reason, the data taken in the reduced temperature range $\leqslant \delta T_C/T_C$ have been left out of the consideration while analysing the data. Several strips of alloy ribbon, all of 3 mm length and 1–2 mm width, were stacked one above the other after a thin layer of Apeizon N grease had been applied in between them to ensure a good thermal contact between the ribbon strips. The sample in the form of a stacked bundle was placed in the sample holder assembly and rotated such that the external magnetic field (H_{ext}) lies within the ribbon plane and is directed along the length of the ribbons. This arrangement minimizes the demagnetizing effects. Sample temperature was monitored by a pre-calibrated platinum sensor which is in body contact (and hence in very good thermal contact) with the sample. The demagnetizing factor N (typically, $N \simeq 0.03$) was computed from the slope of the M (magnetization) versus H_{ext} straight-line (i.e., $4\pi N = (\text{slope})^{-1}$) isotherm taken at a temperature ($T = 77$ K) well below the Curie temperature (T_C) in the field range -20 Oe $\leqslant H_{ext} \leqslant 20$ Oe. T_C was determined to an accuracy of ± 1 K by identifying T_C with the temperature at which a *kink* occurs in the thermomagnetic curve taken at $H_{ext} = 10$ Oe (i.e., by the so-called kink-point method [26]).

M versus H_{ext} isotherms in fields up to 15 kOe for the above-mentioned alloys were taken at $\simeq 0.1$ K (1.0 K) intervals in (outside) the critical region, i.e., in the temperature range $\simeq T_C \pm 15$ K. The temperature interval at which the isotherms were recorded was gradually increased to 5 K for temperatures well above T_C. Each isotherm was obtained by measuring M at 55 predetermined but fixed field values (each stable to within ± 1 Oe) in the

range $0 \leqslant H_{ext} \leqslant 15$ kOe. The temperature was held constant to within ± 25 mK (± 40 mK) for $T \leqslant 300$ K ($T > 300$ K) by means of a proportional, integral and derivative temperature controller. Magnetization measurements were extended to temperatures beyond 300 K only for the alloys with $x = 4$ and 6 since their Curie temperatures lie above 300 K. Now that T_C for the alloy with $x = 6$ has a value ($\simeq 375$ K) that does not lie far below the crystallization temperature ($\simeq 700$ K): before proceeding with the above type of measurement, the sample of this composition was annealed at 450 K for different durations of time till no shift in T_C was observed in the 'kink-point' measurement. This procedure ensured that the specious effects due to structural relaxation did not contaminate the magnetization data recorded in the critical region.

3. Analysis and results

Magnetic order–disorder phase transition at the Curie point (T_C) is characterized by the *asymptotic* critical exponents β, γ and δ as well as by the asymptotic critical amplitudes m_0, (m_0/h_0) and A_0 or D, defined as

$$M(T, 0) = m_0(-\epsilon)^{\beta} \qquad \epsilon < 0 \tag{1}$$

$$\chi_0(T) = \begin{cases} (m_0'/h_0')\epsilon^{-\gamma'} & \epsilon < 0 \\ (m_0/h_0)\epsilon^{-\gamma} & \epsilon > 0 \end{cases} \tag{2}$$

and

$$M(T_C, H) = A_0 H^{1/\delta} \qquad \text{or} \qquad H = DM^{\delta} \qquad \epsilon = 0. \tag{3}$$

In (3) (and in the following text), $H = H_{ext} - 4\pi NM$ denotes the field that the spins constituting the ferromagnetic system actually experience and $D = A_0^{-\delta}$. Strictly speaking, such a power law behaviour ((1) and (2)) is valid only for temperatures extremely close to T_C, i.e., in the limit $|\epsilon| \to 0$. However, in practice, single-power-law fits are frequently attempted on data taken at temperatures not very close to T_C. In this section, we will demonstrate that such fits invariably yield *effective* critical exponents and amplitudes whose values depend on the temperature range chosen for the fit.

With a view to tracing the origin of the spread in the reported exponent values, numerical estimates for the critical exponents and amplitudes have been deduced from the magnetization data taken in the critical region on a-Fe$_{90-x}$Co$_x$Zr$_{10}$($x = 0, 1, 2, 4, 6$) and a-Fe$_{90+y}$Zr$_{10-y}$($y = 0, 1$) alloys using different methods [26] of analysis. These methods fall into two main categories [26]: the scaling equation of state analysis and asymptotic analysis.

3.1. Scaling equation of state analysis

This type of analysis assumes the validity of scaling and makes use of a specific form of scaling equation of state (SES) to simultaneously determine the exponents β and γ (or β and δ) from the 'in-field' magnetization data. In order to ascertain whether or not the results depend on the choice of scaling equation of state, three different forms of SES have been used to analyse the $M(T, H)$ data.

3.1.1. SES I. In this method, use is made of the SES form [26]

$$m = f_{\pm}(h) \tag{4}$$

Table 1. Values of the critical exponents and amplitudes obtained from the SES analyses of the BM data. Numbers in the parentheses denote the uncertainty in the least significant figure and the values of μ_0 are obtained from the values of $M(0, 0)$.

| Conc. (y/x)	Method	T_C (K)	β_{eff}	γ_{eff}	m_0^{eff} (G)	h_0^{eff}/m_0^{eff}	h_0^{eff} (10^5 G)	μ_0 (μ_B)	$\mu_0 h_0^{eff}/k_B T_C$	μ_{eff} (μ_B)	c (%)
$y = 1$	SES II	209.6(1)	0.360(15)	1.380(25)	750(35)	155(50)	1.2(4)	1.34(2)	0.051(20)	44(17)	3(1)
	SES III	209.6(1)	0.360(15)	1.386(20)	835(40)	170(20)	1.4(2)	1.34(2)	0.059(10)	36(8)	4(1)
$y = x = 0$	SES II	225.0(1)	0.350(15)	1.386(30)	800(30)	175(50)	1.4(4)	1.44(2)	0.060(20)	38(14)	4(1)
	SES III	225.0(1)	0.355(15)	1.386(20)	860(50)	215(25)	1.9(3)	1.44(2)	0.081(14)	28(6)	5(1)
$x = 1$	SES II	256.7(1)	0.365(30)	1.380(30)	840(30)	200(75)	1.7(9)	1.52(2)	0.068(20)	35(11)	5(1)
	SES III	256.7(1)	0.365(15)	1.380(15)	860(40)	350(30)	3.0(4)	1.52(2)	0.120(18)	20(4)	8(1)
$x = 2$	SES II	281.6(1)	0.360(10)	1.386(25)	800(30)	250(50)	2.0(5)	1.62(2)	0.077(22)	33(8)	5(1)
	SES III	281.6(1)	0.360(15)	1.386(20)	850(40)	455(50)	3.9(7)	1.62(2)	0.150(28)	17(5)	10(1)
$x = 4$	SES II	328.0(1)	0.355(15)	1.390(25)	900(30)	350(48)	3.2(5)	1.79(2)	0.117(22)	25(4)	7(1)
	SES III	327.9(1)	0.358(15)	1.390(20)	955(60)	580(55)	5.5(8)	1.79(2)	0.202(30)	14(3)	13(1)
$x = 6$	SES II	374.8(1)	0.355(10)	1.386(25)	950(30)	500(50)	4.8(6)	1.81(2)	0.156(22)	19(3)	10(1)
	SES III	374.7(1)	0.360(15)	1.386(15)	935(60)	655(75)	6.1(9)	1.81(2)	0.198(30)	14(3)	13(1)
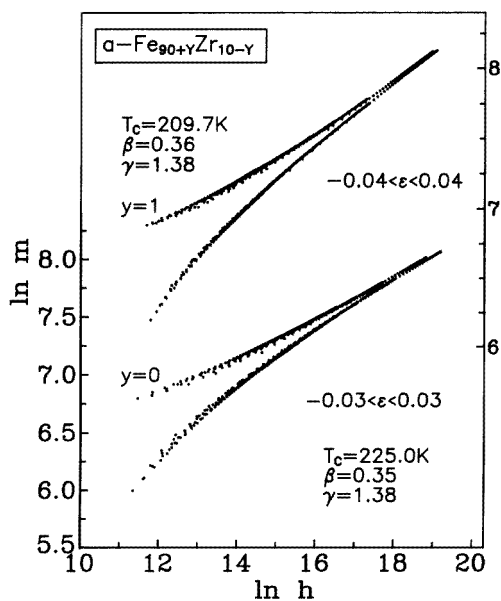
Figure 1. A $\ln(m \equiv M/|\epsilon|^{\beta})$ versus $\ln(h \equiv H/|\epsilon|^{\beta+\gamma})$ scaling plot, based on SES I, for a-Fe$_{90+y}$Zr$_{10-y}$ alloys. Note that the ordinate scales on the left- and right-hand sides pertain to the scaling plots for the alloys with $y = 0$ and 1, respectively. In these plots, the upper (lower) curve represents the *universal* curve $f_{-}(h)$ $(f_{+}(h))$ onto which the M–H isotherms taken at temperatures $\epsilon < 0$ $(\epsilon > 0)$ collapse (see text). The inequality, e.g., $-0.03 \lesssim \epsilon \lesssim 0.03$ for the alloy with $y = 0$, specifies the temperature range around T_C covered by the universal curves for a given composition.

where $f_{+}(h)$ and $f_{-}(h)$ are the scaling functions [26] for temperatures above and below T_C, while $m \equiv M/|\epsilon|^{\beta}$ and $h \equiv H/|\epsilon|^{\beta+\gamma}$ are the scaled magnetization and the scaled field, respectively. In accordance with (4), the M–H isotherms in the critical region are made to fall onto two universal curves, (f_{-} for $\epsilon < 0$ and f_{+} for $\epsilon > 0$) through a proper choice [4, 5, 8, 9, 21–23, 26] of the parameters T_C, β and γ. A representative $\ln m$–$\ln h$ plot that illustrates such a scaling behaviour of the magnetization is shown in figure 1. However, this choice is by no means unique in the sense that nearly the same quality of data collapse, onto two universal curves can be achieved for a wide range of parameter values (typically, $\pm 2\%$ for T_C and $\pm 10\%$ for β and γ), particularly when the data outside the asymptotic critical region are also included in the analysis. This problem can be tackled to some extent by employing the range-of-fit SES analysis [27] in which more and more of the data taken at temperatures away from T_C are excluded from the m–h plot so that the exponents β and γ become increasingly sensitive to the choice of T_C and the data exhibit strong departures from the curves $f_{-}(h)$ and $f_{+}(h)$ if the choice of the parameters differs from the correct one. Were it not for the insensitive nature of the log–log scale, this procedure would go on refining the values of the critical exponents until they approached the asymptotic values. Thus, one obtains only the effective critical exponents by this method and their values depend on the temperature range over which this analysis is attempted.

3.1.2. SES II. We now use an alternative form of scaling equation of state given by

$$m^2 = \mp a_{\pm} + b_{\pm}(h/m) \tag{5}$$

(where the plus and minus signs have the same meaning as stated above and the constants $a_\pm$ and $b_\pm$ are related to the critical amplitudes as $m_0 = \sqrt{a_-}$ and $h_0/m_0 = a_+/b_+$) to determine the exponents β and γ. In this case too, the M–H isotherms in the critical region are made to fall onto two universal curves, one below T_C and the other above T_C, in an m^2–h/m plot, through a proper choice of the parameters T_C, β and γ. This form of SES has the distinction of providing more accurate estimates for T_C, β and γ when the range-of-fit analysis is used since even the slight deviations of the data from the universal curves, which do not show up clearly in a $\ln m$–$\ln h$ plot because of the insensitive nature of the double-logarithmic scale, become easily discernible in the m^2–h/m plot. Another advantage of SES II (5) is that it allows estimation of the critical amplitudes (m_0 and h_0/m_0) from the intercepts made by the universal curves on the m^2 and h/m axes. m^2–h/m plots for different compositions in the two alloy series in a narrow temperature range $-0.008 \lesssim \epsilon \lesssim 0.008$ around T_C are shown in figure 2 while the average values of T_C, β, γ, m_0 and h_0/m_0 obtained in this temperature range are listed in table 1. The critical exponents and amplitudes even in such a narrow temperature range do not attain their asymptotic values but instead possess effective values, which vary within the limits specified in table 1 when the temperature range is progressively narrowed down further in the range-of-fit analysis.

3.1.3. SES III. This method is based on the Arrott–Noakes equation of state [28], i.e.,

$$(H/M)^{1/\gamma} = a'\epsilon + b'M^{1/\beta}. \tag{6}$$

In (6), the temperature-independent coefficients a' and b' are related to the critical amplitudes m_0, m_0/h_0 and D, appearing in (1)–(3), as

$$m_0 = (a'/b')^\beta \qquad (m_0/h_0) = (a')^{-\gamma} \qquad D = (b')^\gamma. \tag{7}$$

In this method, the M–H isotherms taken at different temperatures in the critical region are used to construct the $M^{1/\beta}$–$(H/M)^{1/\gamma}$ plot, the so-called modified Arrott plot (MAP), and the values of critical exponents β and γ are varied so as to make these isotherms linear over as wide a range of H/M values as possible and parallel to one another in a narrow temperature range around T_C (with the critical isotherm at T_C passing through the origin). The critical exponents obtained in this way are still effective exponents. However, the values for critical exponents and amplitudes very close to the asymptotic ones are obtained if during the course of this analysis, the temperature range around T_C is narrowed down to such an extent that T_C is approached closer than $|\epsilon| \simeq 10^{-3}$. Values of the exponents and amplitudes (calculated at $\epsilon \simeq 0.01$) obtained from the modified Arrott plots (MAPs) thus constructed for a-Fe$_{90-x}$Co$_x$Zr$_{10}$ ($x = 0, 1, 2, 4$ and 6) and a-Fe$_{90+y}$Zr$_{10-y}$($y = 0, 1$) alloys are listed in table 1 and a representative MAP is shown in figure 3. In this figure, only the isotherms at a few selected temperatures in the critical region are included for the sake of clarity. The $M(T, H)$ data are observed to significantly deviate from the linear MAP isotherms at low fields for temperatures away from T_C and such deviations become more pronounced as $|T - T_C|$ increases. The origin of such deviations is not clear at present. Unlike the previous two methods of analysis, the SES III data analysis yields more accurate values for T_C, β and γ because only *two* (as against *three* in the SES I and II analyses) free parameters are involved and permits accurate determination of the 'zero-field' quantities such as spontaneous magnetization, $M(T, 0)$, and initial susceptibility, $\chi_0(T)$, from the intercepts $[M(T, 0)]^{1/\beta}$ and $[\chi_0^{-1}(T)]^{1/\gamma}$ that MAP isotherms make on the ordinate for $T \lesssim T_C$ and on the abscissa for $T \gtrsim T_C$, respectively, when their high-field linear portions are extrapolated to $(H/M)^{1/\gamma} = 0$ and $M^{1/\beta} = 0$. The $M(T, 0)$ and $\chi_0^{-1}(T)$ data, computed
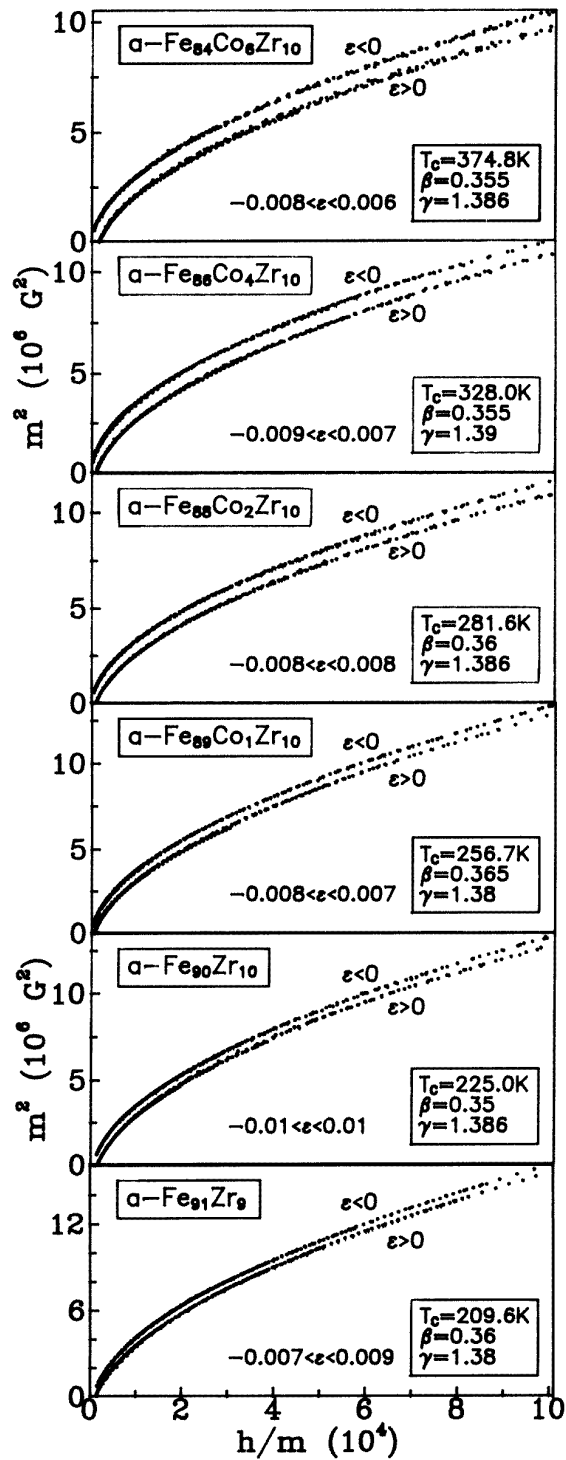
Figure 2. m^2–h/m scaling plots based on SES II for a-Fe$_{90-x}$Co$_x$Zr$_{10}$ and a-Fe$_{90+y}$Zr$_{10-y}$ alloys. The inequality, e.g., $-0.01 \lesssim \epsilon \lesssim 0.01$ for a-Fe$_{90}$Zr$_{10}$, specifies the temperature range around T_C covered by the universal curves (see the text) for a given composition.

from these intercepts, are plotted against $\epsilon = (T - T_C)/T_C$ in figures 4 and 5, respectively, and analysed using the asymptotic methods described below.
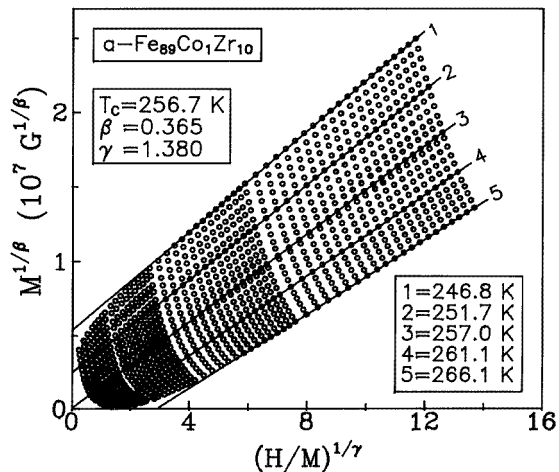

Figure 3. A MAP for a-Fe$_{89}$Co$_1$Zr$_{10}$ alloy in the critical region.

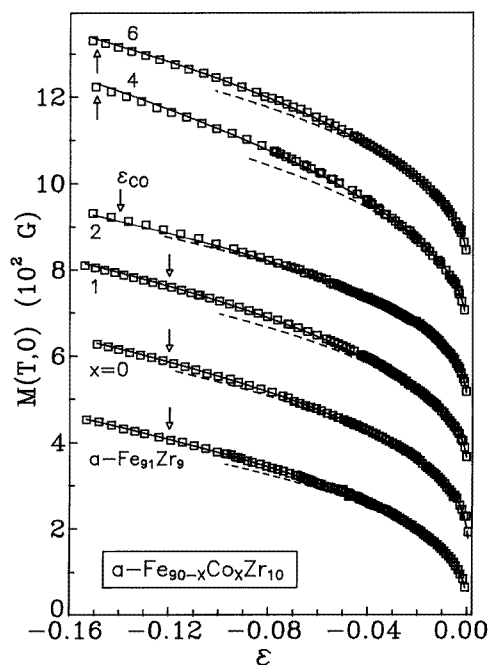**Figure 4.** $M(T, 0)$ plotted against $\epsilon = (T - T_C)/T_C$ in the critical region. Note that $M(T, 0)$ data for $x = 0$, 1, 2, 4 and 6 are shifted up by the amount 155, 310, 465, 620 and 775 G, respectively, with respect to those for a-Fe$_{91}$Zr$_9$. The dashed and continuous curves through the data points represent the best least-squares fits based on equations (8) and (12) or (14) of the text, respectively.

Figure 5. $\chi_0^{-1}(T)$ plotted against $\epsilon = (T - T_C)/T_C$ in the critical region. Note that χ_0^{-1} data for $x = 0, 1, 2, 4$ and 6 are shifted up by the amount $1.27, 2.54, 3.81, 5.08$ and 6.35, respectively, with respect to those for a-Fe$_{91}$Zr$_9$. The dashed and continuous curves through the data points represent the best least-squares fits based on equations (9) and (13) or (15) of the text, respectively.
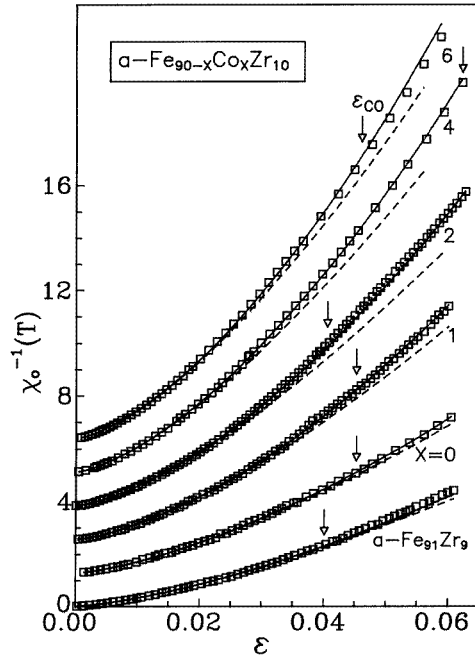
3.2. Asymptotic analysis

3.2.1. Single-power-law (SPL) analysis. The spontaneous magnetization and initial susceptibility data in the critical region have been directly fitted to (1) and (2) with asymptotic critical exponents and amplitudes in these replaced by their effective counterparts β_{eff}, γ_{eff}, m_0^{eff} and $(m_0/h_0)^{eff}$, i.e., to the single-power-law expressions

$$M(T, 0) = m_0^{eff}(-\epsilon)^{\beta_{eff}} \qquad \epsilon < 0 \tag{8}$$

and

$$\chi_0(T) = (m_0/h_0)^{eff}\epsilon^{-\gamma_{eff}} \qquad \epsilon > 0. \tag{9}$$

A detailed range-of-fit analysis of $M(T, 0)$ and $\chi_0(T)$ data based on the above expressions indicates that the values of critical exponents and amplitudes depend on the temperature range chosen for the analysis. The dashed curves in figures 4 and 5 represent the best theoretical fits based on (8) and (9) over the temperature range $|\epsilon| \leqslant 0.02$ with the choice of the parameters given in table 2.

3.2.2. The Kouvel–Fisher (KF) method. The Kouvel–Fisher (KF) method [25] is based on the single power laws, (8) and (9), and determines critical exponents through analytical means by rewriting (8) and (9) in the form

$$Y(T) = M(T, 0)|\,\mathrm{d}M(T, 0)/\mathrm{d}T|^{-1} = (T - T_C)/\beta_{eff} \tag{10}$$

Table 2. Results of the Kouvel–Fisher (KF) and single-power-law (SPL) analyses of the $M(T, 0)$ and $\chi_0(T)$ recorded on the a-$Fe_{90-x}Co_xZr_{10}$ and a-$Fe_{90+y}Zr_{10-y}$ alloys.

Alloy conc.	Analysis	Fit range $(10^3|\epsilon|)$	T_C^- (K)	β_{eff}	m_0^{eff} (G)	T_C^+ (K)	γ_{eff}	$(m_0/h_0)^{eff}$ (10^{-3})
$y = 1$	KF	0.7–10	209.7(1)	0.38(2)	870(30)	209.6(1)	1.40(2)	4.95(5)
	KF	0.8–20	209.7(1)	0.39(2)	905(30)	209.6(1)	1.42(2)	4.65(5)
	KF	1.0–40	209.8(1)	0.41(2)	950(30)	209.6(1)	1.43(2)	4.35(5)
	SPL	0.9–10	209.8(1)	0.39(2)	850(40)	209.6(1)	1.40(2)	4.90(10)
	SPL	1.0–20	209.8(1)	0.40(2)	935(40)	209.6(1)	1.42(2)	4.60(10)
$y = 0;$	KF	0.6–10	225.0(1)	0.38(2)	870(35)	225.0(1)	1.41(2)	3.50(10)
$x = 0$	KF	0.7–20	225.0(1)	0.39(2)	905(35)	225.0(1)	1.44(2)	3.05(10)
	KF	1.0–40	225.1(1)	0.41(2)	950(35)	224.9(1)	1.47(2)	2.80(10)
	SPL	0.7–10	225.0(1)	0.37(2)	840(50)	224.9(1)	1.41(2)	3.50(15)
	SPL	0.8–20	225.1(1)	0.40(2)	950(50)	224.9(1)	1.44(2)	3.10(15)
$x = 1$	KF	0.6–10	256.8(1)	0.38(2)	925(35)	256.6(1)	1.42(3)	2.45(10)
	KF	0.6–20	256.8(1)	0.40(2)	995(35)	256.6(1)	1.44(3)	2.25(10)
	KF	0.6–40	256.8(1)	0.41(2)	1060(35)	256.7(1)	1.47(3)	1.90(10)
	SPL	0.5–10	256.7(2)	0.39(2)	940(50)	256.7(2)	1.41(2)	2.30(12)
	SPL	0.7–20	256.8(2)	0.41(2)	1035(50)	256.7(2)	1.44(2)	2.20(12)
$x = 2$	KF	0.7–10	281.6(1)	0.38(2)	915(35)	281.6(1)	1.39(2)	2.05(8)
	KF	0.8–20	281.6(1)	0.38(2)	935(35)	281.6(1)	1.43(2)	1.75(8)
	KF	1.0–40	281.7(1)	0.39(2)	950(35)	281.5(1)	1.49(2)	1.35(8)
	SPL	0.6–10	281.5(1)	0.37(2)	875(50)	281.6(1)	1.39(2)	1.95(10)
	SPL	0.7–20	281.6(1)	0.38(2)	950(40)	281.6(1)	1.42(2)	1.80(10)
$x = 4$	KF	0.4–10	328.0(1)	0.39(2)	1130(35)	328.0(1)	1.41(2)	1.60(8)
	KF	0.5–20	328.0(1)	0.40(2)	1195(35)	328.0(1)	1.43(2)	1.40(8)
	KF	0.8–40	328.1(1)	0.42(2)	1260(35)	327.9(1)	1.48(2)	1.15(8)
	SPL	0.4–10	328.0(1)	0.38(2)	1150(50)	328.0(1)	1.40(3)	1.55(15)
	SPL	0.4–20	327.9(1)	0.40(2)	1170(50)	328.0(1)	1.43(3)	1.40(15)
$x = 6$	KF	0.4–10	374.8(1)	0.39(2)	1095(35)	374.8(1)	1.40(2)	1.36(6)
	KF	0.4–20	374.8(1)	0.40(2)	1130(35)	374.8(1)	1.42(2)	1.20(6)
	KF	0.6–40	374.9(1)	0.42(2)	1190(35)	374.8(1)	1.47(2)	0.98(6)
	SPL	0.5–10	374.8(2)	0.38(2)	1090(50)	374.7(2)	1.40(3)	1.40(12)
	SPL	0.5–20	374.8(2)	0.40(2)	1105(50)	374.7(2)	1.43(3)	1.25(12)

and

$$X(T) = \chi_0^{-1}(T)|\,d\chi_0^{-1}(T)/dT|^{-1} = (T - T_C)/\gamma_{eff}. \tag{11}$$

According to this approach [25], in the asymptotic critical region where (8) and (9) (and hence (10) and (11)) are valid, $Y(T)$ against T ($X(T)$ against T) plot should be a straight line with slope $1/\beta_{eff}(1/\gamma_{eff})$ and intercept on the T-axis equal to T_C^- (T_C^+). The $Y(T)$ and $X(T)$ data plotted against ϵ in figures 6 and 7 demonstrate the validity of the KF approach for the alloys investigated. In these figures, $Y(T)$ and $X(T)$ have been displayed as functions of reduced temperature ϵ, instead of T, so as to accommodate such plots for compositions with widely different T_C values in a single graph. The straight lines through the data points represent the least-squares fits, based on (10) or (11), over the ϵ range indicated by the upward arrows. The values for β_{eff}, γ_{eff} and T_C in different temperature ranges for the alloys in question obtained by the KF method are listed in table 2. The entries

in this table clearly show that the results of the KF analysis are in very good agreement with those of the single-power-law analysis and that the *effective* exponents and/or amplitudes *depend* on the temperature range used for the fit.
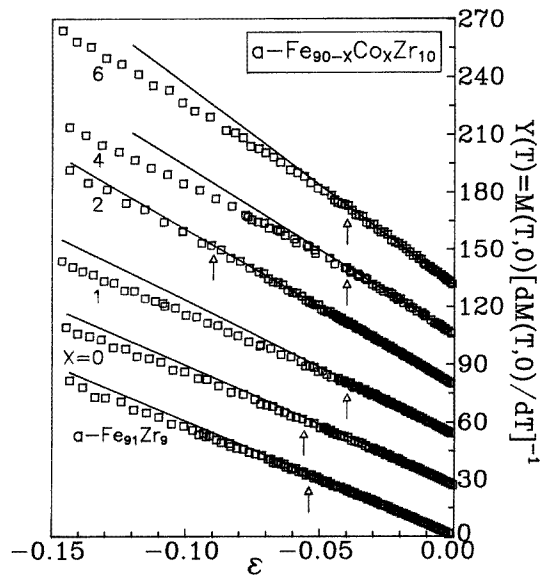

Figure 6. $Y(T)$ plotted against ϵ in the critical region. The zero on the ordinate scale for $x = 0$, 1, 2, 4 and 6 is shifted up by the amount 26.25, 52.5, 78.75, 105.0 and 131.25, respectively, with respect to that of a-Fe$_{91}$Zr$_9$. The straight lines through the data points represent the best least-squares fits based on equation (10) of the text over the ϵ ranges indicated by the upward arrows.

3.2.3. Analysis with 'correction-to-scaling' (CTS) terms. In view of the fact that all the methods of analysis considered so far are based on single power laws and yet, with the exception of the MAP method, they have been used to analyse data in temperature ranges (around T_C) that are not too narrow, the values of exponents and amplitudes so determined are nothing but the *effective* values. In order to determine the true *asymptotic* values of the critical exponents and amplitudes, the expressions for $M(T, 0)$ and $\chi_0(T)$ valid in the asymptotic critical region should include the 'correction-to-scaling' (CTS) terms arising from nonlinear irrelevant scaling fields, as predicted by the RG theories [13–16, 29, 30]. The expressions that are valid for amorphous ferromagnets and retain only the leading CTS terms have the form [13–16, 20–23, 30]

$$M(T, 0) = m_0(-\epsilon)^\beta[1 + a_{M_1}^-|\epsilon|^{\Delta_1} + a_{M_2}^-|\epsilon|^{\Delta_2}] \qquad \epsilon < 0 \qquad (12)$$

and

$$\chi_0(T) = (m_0/h_0)\epsilon^{-\gamma}[1 + a_{\chi_1}^+|\epsilon|^{\Delta_1} + a_{\chi_2}^+|\epsilon|^{\Delta_2}] \qquad \epsilon > 0 \qquad (13)$$

where Δ_1 and Δ_2 and $(a_{M_1}^-, a_{M_2}^-)$ and $(a_{\chi_1}^+, a_{\chi_2}^+)$ are the leading CTS critical exponents and amplitudes, respectively, while the remaining quantities have the same meanings as stated earlier. Note that in the case of crystalline ferromagnets the expressions for $M(T, 0)$ and $\chi_0(T)$ have the terms with factor $|\epsilon|^{\Delta_2}$ as the first leading correction term because the CTS terms $a_{M_1}^-|\epsilon|^{\Delta_1}$ and $a_{\chi_1}^+|\epsilon|^{\Delta_1}$ are absent. By virtue of the fact that: [13–16, 18, 20–23, 29]
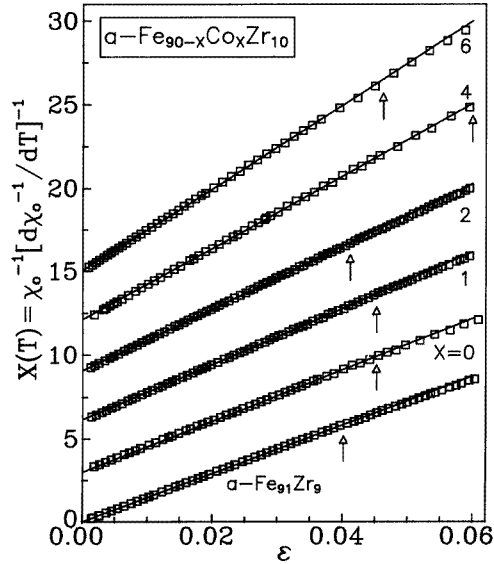
Figure 7. $X(T)$ plotted against ϵ in the critical region. The zero on the ordinate scale for $x = 0$, 1, 2, 4 and 6 is shifted up by the amount 3.0, 6.0, 9.0, 12.0 and 15.0, respectively. The straight lines through the data points represent the best least-squares fits based on equation (11) of the text over the ϵ ranges indicated by the upward arrows.

$\Delta_1 \ll \Delta_2$, the CTS terms in (12) and (13) involving the exponent Δ_1 are significant only for temperatures in the immediate vicinity of T_C whereas the CTS terms containing the factor $|\epsilon|^{\Delta_2}$ dominate for temperatures well within the asymptotic critical region but away from T_C. In order to accurately determine these correction terms, the following procedure has been adopted. First, the amplitudes $a_{M_2}^-$ and $a_{\chi_2}^+$ are set equal to zero and a detailed 'range-of-fit' analysis of the $M(T, 0)$ ($\chi_0(T)$) data, based on the modified version of (12) ((13)) that includes the first correction term only, is carried out with the help of a nonlinear least-squares fit computer program which treats m_0, T_C^-, β and $a_{M_1}^-$ ((m_0/h_0), γ, T_C^+ and $a_{\chi_1}^+$) as free fitting parameters and keeps the CTS exponent Δ_1 fixed at the theoretically predicted [16, 18, 31] value of $\Delta_1 = 0.11$. In the 'range-of-fit' analysis, the lower bound $|\epsilon_{min}|$ of the temperature range $|\epsilon_{min}| \leqslant |\epsilon| \leqslant |\epsilon_{max}|$ is fixed at $|\epsilon_{min}| \approx 0$ while the upper bound $|\epsilon_{max}|$ is increased so as to include more and more data points for temperatures away from T_C. Such an exercise reveals that over a certain temperature range close to T_C, the values of all the parameters including the coefficient $a_{M_1}^-$ or $a_{\chi_1}^+$ are essentially unaffected by the variation in $|\epsilon_{max}|$. Next, the coefficient of the first CTS term $a_{M_1}^-(a_{\chi_1}^+)$ is fixed at this value and the 'range-of-fit' analysis of $M(T, 0)(\chi_0(T))$ data is carried out by using (12) ((13)) with both the correction terms included and treating m_0, T_C^-, β and $a_{M_2}^-$((m_0/h_0), T_C^+, γ and $a_{\chi_2}^+$) as free fitting parameters while keeping Δ_1 and Δ_2 fixed at [16, 18, 20–23, 31] $\Delta_1 = 0.11$ and $\Delta_2 = 0.55$. The quality of the least-squares (LS) fits obtained in this way (henceforth referred to as the CTS analysis) is far superior to that of the single-power-law fits in the same temperature range, as inferred from the substantially lower sum of deviation squares, χ_r^2, and from the deviation plots. Figure 8 shows the deviation plots for a-$Fe_{91}Zr_9$ and a-$Fe_{90}Zr_{10}$ alloys in which the percentage deviation of the $M(T, 0)$ or $\chi_0^{-1}(T)$ data from the corresponding theoretical values deduced from the best LS fit, i.e., $100[M(\text{exp}) - M(\text{fit})]/M(\text{exp})$ or $100[\chi_0^{-1}(\text{exp}) - \chi_0^{-1}(\text{fit})]/\chi_0^{-1}(\text{exp})$, is plotted against

ϵ. This figure clearly demonstrates the superiority of the CTS fits over the KF (or SPL) fits in the asymptotic critical region in that the former type of fit closely reproduces the observed variation of $M(T, 0)$ and $\chi_0(T)$ with T over a wider temperature range (especially so for temperatures in the immediate vicinity of T_C) whereas the latter type of fit presents *systematic* deviations. The deviation plots for $\chi_0^{-1}(T)$ as well as $M(T, 0)$ data for all the remaining alloys are similar to those shown in figure 8. The CTS analysis, apart from yielding accurate values for the asymptotic critical exponents and amplitudes, reveals that the values of these exponents and amplitudes do not change (within the error limits) as the temperature range for the CTS fit is varied in the 'range-of-fit' analysis. The maximum value of $|\epsilon_{max}|$ up to which the CTS fits yield stable values for all the parameters marks the crossover temperature $\epsilon_{co}^-(\epsilon < 0)$ and $\epsilon_{co}^+(\epsilon > 0)$ for $M(T, 0)$ and $\chi_0(T)$, respectively, while $\epsilon_{co}^- \leqslant \epsilon \leqslant \epsilon_{co}^+$ gives the extent of the asymptotic critical region (ACR). The theoretical fits, based on (12) and (13), in the ACR with the values of parameters given in tables 3 and 4 (which also include critical amplitude values calculated for the isotherm closest to T_C from (7) and those of critical exponents obtained by the MAP analysis), are shown as continuous curves in figures 4 and 5. In these figures, the crossover temperatures $\epsilon_{co}^\pm$ are indicated by downward arrows. It is noticed from tables 3 and 4 that the values of T_C^- and T_C^+ are in good agreement with one another within the uncertainty limits, the asymptotic critical exponents are *composition independent* and the MAP analysis yields values for critical exponents and amplitudes that are close to their asymptotic values.

Table 3. Results of the CTS and MAP analyses of the $M(T, 0)$ data.

Alloy conc.	Method	Fit range $(10^3|\epsilon|)$	T_C^- (K)	β	m_0 (G)	$a_{M_1}^-$	$a_{M_2}^-$
$y = 1$	CTS	0.94–115	209.68(3)	0.366(4)	795(15)	−0.03(1)	0.52(8)
	MAP			0.360(15)	810(40)		
$x = y = 0$	CTS	0.52–115	225.02(4)	0.360(5)	830(25)	−0.05(1)	0.85(15)
	MAP			0.355(15)	835(50)		
$x = 1$	CTS	0.54–120	256.69(5)	0.368(6)	840(25)	−0.04(1)	0.80(10)
	MAP			0.365(15)	860(40)		
$x = 2$	CTS	0.46–137	281.57(5)	0.363(5)	870(25)	−0.04(1)	0.65(10)
	MAP			0.360(15)	860(40)		
$x = 4$	CTS	0.23–137	327.90(6)	0.365(6)	1000(20)	−0.06(1)	0.90(10)
	MAP			0.358(15)	950(60)		
$x = 6$	CTS	0.01–151	374.75(5)	0.370(5)	950(25)	−0.05(1)	0.70(8)
	MAP			0.360(15)	910(60)		

3.2.4. Analysis using nonlinear scaling variables. All the methods of analysis employed until now have been based on the expressions that involve the linear variables ϵ and H. Such expressions, e.g., (12) and (13), provide the best theoretical fits to the $M(T, 0)$ and $\chi_0(T)$ data in the ACR only. However, the quality of these fits deteriorates considerably for temperatures outside the ACR. Such a behaviour has been previously observed [4, 5, 20–23, 26, 27, 32–34] in many crystalline and amorphous ferromagnets. However, nearly a decade ago, Souletie and Tholence [35] have found that $\chi_0(T)$ data of crystalline Ni are
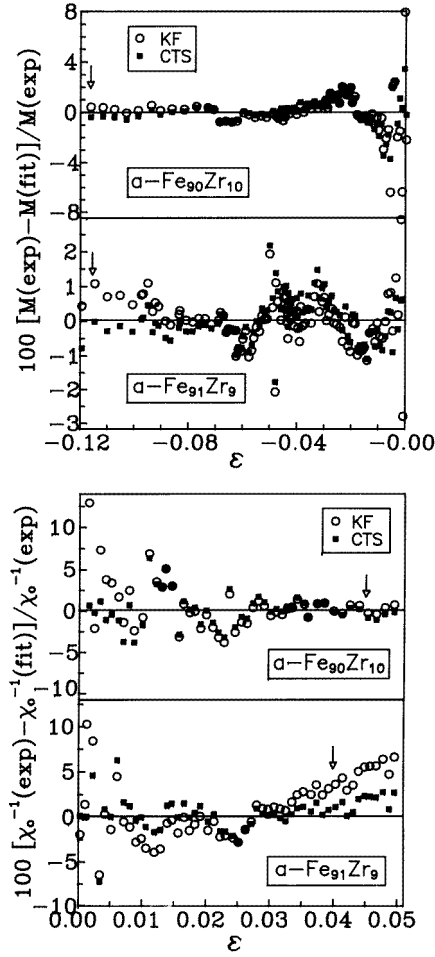
Figure 8. The percentage deviation of the $M(T,0)$ and $\chi_0^{-1}(T)$ data from the theoretical values corresponding to the LS fits obtained from the KF and CTS data analyses for $T < T_C$ and $T > T_C$, respectively. Downward arrows mark the extent of the asymptotic critical region.

described by a power law of the form $\chi_0(T) = A_\chi T^{-1}\tilde{\epsilon}^{-\gamma} + B_\chi$, in the nonlinear (NL) variable $\tilde{\epsilon} = (T - T_C)/T$ (generally referred to as the modified Curie–Weiss law) over an incredibly large temperature range of T_C to $3T_C$. A theoretical treatment [36] (the so-called NL scaling theory) that, besides making use of the renormalization group ideas and NL scaling variables $\tilde{\epsilon} = (t - 1)/t$ and $\tilde{h} = H/t$ ($t = T/T_C$), takes into account both NL irrelevant as well as relevant scaling fields has provided a firm theoretical basis for this power law. Now that the recent investigations [22, 36, 37] of the critical behaviour of certain ferromagnetic systems over a wide temperature range vindicate the nonlinear scaling approach [36], a detailed analysis of $M(T,0)$ and $\chi_0(T)$ data has been carried out based on the expressions, predicted by this theory, that either include the leading *nonanalytic corrections*, arising from NL *irrelevant* scaling fields, i.e.,

$$M(T,0) = \tilde{m}_0|\tilde{\epsilon}|^\beta[1 + \tilde{a}_{M_1}^-|\tilde{\epsilon}|^{\Delta_1} + \tilde{a}_{M_2}^-|\tilde{\epsilon}|^{\Delta_2}] \qquad \tilde{\epsilon} < 0 \qquad (14)$$

$$\chi_0(T) = (\tilde{m}_0/\tilde{h}_0)t^{-1}|\tilde{\epsilon}|^{-\gamma}[1 + \tilde{a}_{\chi_1}^+|\tilde{\epsilon}|^{\Delta_1} + \tilde{a}_{\chi_2}^+|\tilde{\epsilon}|^{\Delta_2}] \qquad \tilde{\epsilon} > 0 \qquad (15)$$

Table 4. Results of the CTS and MAP analyses of the $\chi_0(T)$ data.

Alloy conc.	Method	Fit range $(10^3|\epsilon|)$	T_C^+ (K)	γ	m_0/h_0 (10^{-3})	$a_{\chi_1}^+$	$a_{\chi_2}^+$
$y = 1$	CTS	0.39–41	209.63(3)	1.383(4)	5.7(3)	−0.03(1)	−0.5(1)
	MAP			1.386(20)	6.5(5)		
$x = y = 0$	CTS	0.78–45	224.97(4)	1.390(5)	4.3(2)	−0.05(1)	−0.8(1)
	MAP			1.386(20)	4.6(5)		
$x = 1$	CTS	0.37–45	256.66(5)	1.385(5)	3.2(2)	−0.05(2)	−1.0(2)
	MAP			1.380(15)	3.0(3)		
$x = 2$	CTS	0.05–41	281.61(5)	1.389(6)	2.2(1)	−0.05(2)	−1.0(3)
	MAP			1.386(20)	2.5(3)		
$x = 4$	CTS	0.45–62	327.98(6)	1.383(7)	1.9(1)	−0.05(2)	−1.1(3)
	MAP			1.390(20)	2.0(2)		
$x = 6$	CTS	0.86–46	374.72(5)	1.386(6)	1.6(1)	−0.05(2)	−1.0(2)
	MAP			1.386(15)	1.6(2)		

or *analytic corrections*, originating from NL *relevant* scaling fields, i.e.,

$$M(T,0) = B_M|\tilde{\epsilon}|^{\beta}[1 + \tilde{a}_M^-\tilde{\epsilon}] \qquad \tilde{\epsilon} < 0 \tag{16}$$

$$\chi_0(T) = A_\chi t^{-1}|\tilde{\epsilon}|^{-\gamma}[1 + \tilde{a}_\chi^+\tilde{\epsilon}] \qquad \tilde{\epsilon} > 0. \tag{17}$$

Using the same extrapolation procedure as described in section 3.2.3, $M(T,0)$ and $\chi_0(T)$ have been extracted from the MAP isotherms, constructed in a temperature range as wide as $0.3T_C \lesssim T \lesssim 1.5T_C$ using the values of exponents β and γ obtained in the critical region. One such MAP for a-Fe$_{91}$Zr$_9$, constructed from a few selected M–H isotherms taken in the range 68–300 K, is shown in figure 9. This figure captures all the essential features of the MAPs for the remaining compositions. Detailed analysis of the $M(T,0)$ and $\chi_0(T)$ data (figures 10 and 11) based on (14)–(17) reveals that in the asymptotic critical region (ACR), (14) and (15) reproduce the $M(T,0)$ and $\chi_0(T)$ data to far greater accuracy than (16) and (17). Note that in the theoretical fits based on (14) and (15), the CTS exponents are kept fixed at their theoretical values $\Delta_1 = 0.11$ and $\Delta_2 = 0.55$ as was earlier the case with the CTS analysis involving linear variables ϵ and H. In the ACR, the CTS analysis, based on the expressions that include the non-analytic correction terms alone, yields the *same* results regardless of whether these correction terms are expressed in *linear* scaling variables, (12) and (13), or in *nonlinear* scaling variables, (14) and (15). On the other hand, (16) and (17), which include a single leading analytic correction term, provide very good overall fits in temperature ranges as wide as $0.45T_C \lesssim T \lesssim T_C$ for $M(T,0)$ and $T_C \lesssim T \lesssim 1.5T_C$ for $\chi_0(T)$ for all the alloys in question with the values of fit parameters and fit ranges given in tables 5 and 6. These fits are represented by continuous curves in figures 10 and 11. In view of the claim [35] that for crystalline Ni the empirical relation

$$\chi_0(T) = A_\chi t^{-1}|\tilde{\epsilon}|^{-\gamma} + B_\chi \qquad \tilde{\epsilon} > 0 \tag{18}$$

with the background correction term B_χ describes very well the observed variation of χ_0 with T from T_C to $3T_C$, (18) has been used to analyse the $\chi_0(T)$ data over the entire temperature range. This exercise shows that even though (18) with $B_\chi \neq 0$ provides a slightly better fit
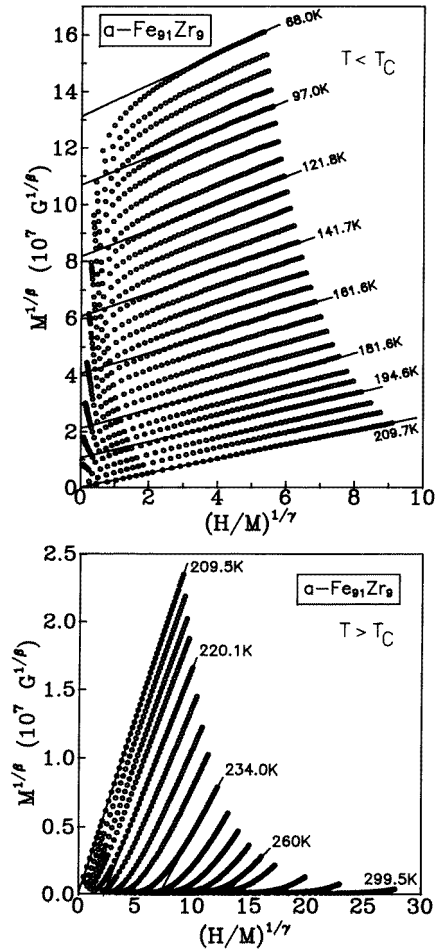
Figure 9. A MAP for a-Fe$_{91}$Zr$_9$ over a wide temperature range for $T < T_C$ and $T > T_C$; $\beta = 0.36$ and $\gamma = 1.386$.

than when $B_\chi = 0$ in (18), it *does not* reproduce the observed temperature variation of χ_0 as closely as (17) does. The deviation plot shown in figure 12 for a-Fe$_{90+y}$Zr$_{10-y}$($y = 0, 1$) alloys testifies to the correctness of this inference in that the percentage deviation for the fits based on (17) is considerably smaller than that for the fits based on (18) in the entire temperature range (even for temperatures close to T_C). However, neither of these expressions (i.e., (17) and (18)) correctly describes the actual functional form of $\chi_0(T)$ in the ACR, as inferred from large systematic deviations of the theoretical values from the observed ones in the ACR (figure 12). By comparison, the expression that includes the nonanalytic correction terms either in linear variables (13) or in nonlinear variables (15) provides a much better description of $\chi_0(T)$ in the ACR (figure 8).

3.3. Critical isotherm

The critical exponent δ characterizing the $M(T, H)$ versus H isotherm at $T = T_C$ (the critical isotherm) is obtained by analysing the M–H isotherms in the immediate vicinity
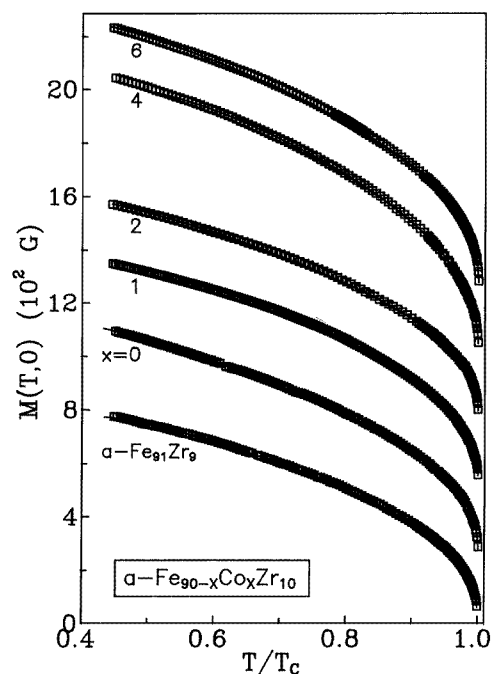
Figure 10. $M(T, 0)$ plotted against T/T_C over a wide temperature range for $T < T_C$. Note that the zero on the ordinate scale for $x = 0, 1, 2, 4$ and 6 is shifted by 250, 500, 750, 1000 and 1250, respectively, and the solid curves represent the least-squares fits based on equation (16).

Table 5. Parameter values for the LS fits, based on equation (16) of the text, to the $M(T, 0)$ data taken over a wide temperature range.

Alloy conc.	Fit range (T/T_C)	T_C^- (K)	β	B_M (G)	$\tilde{a}_M^-$
$y = 1$	0.45–1.0	209.68(8)	0.380(10)	885(30)	−0.15(3)
$x = y = 0$	0.45–1.0	225.10(10)	0.390(15)	970(30)	−0.20(3)
$x = 1$	0.50–1.0	256.72(8)	0.395(10)	1000(30)	−0.22(3)
$x = 2$	0.45–1.0	281.59(10)	0.380(10)	1030(30)	−0.14(3)
$x = 4$	0.50–1.0	327.95(10)	0.395(15)	1230(30)	−0.20(4)
$x = 6$	0.45–1.0	374.70(10)	0.385(10)	1100(30)	−0.13(3)

of T_C in terms of (3). It is evident from (3) that the plot of $\ln M$ against $\ln H$ at $T = T_C$ should be a straight line with slope δ^{-1} and intercept on the ordinate equal to $\ln A_0$. Such $\ln M$–$\ln H$ plots, constructed using the M–H isotherms in the immediate vicinity of T_C for the alloys investigated (figure 13), clearly demonstrate that the isotherm at T_C is indeed a straight line and the isotherms on either side of T_C exhibit a concave-upward and concave-downward curvature for $T < T_C$ and $T > T_C$, respectively. The curvature becomes more pronounced as the temperature increasingly deviates from T_C. These features, characteristic of many amorphous as well as crystalline ferromagnets [5, 22, 23, 27, 33, 34, 37], are clearly borne out by the data presented in figure 13. The solid line in figure 13 for each composition represents the theoretical fit based on (3) to the critical isotherm at T_C. The exponent δ and amplitude A_0 or D are computed from the slope and intercept on the ordinate of this

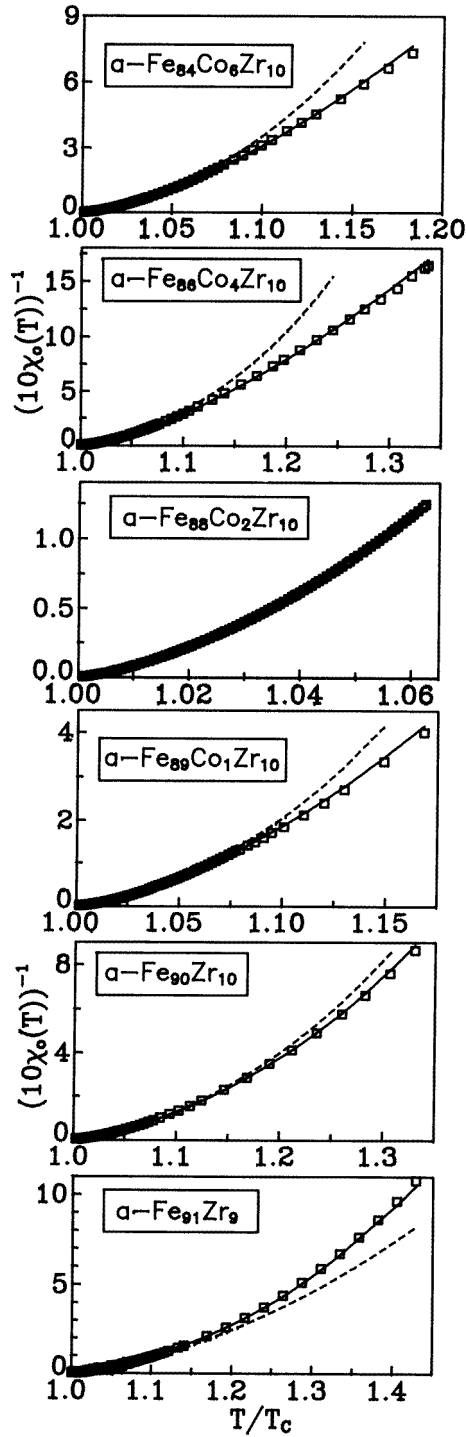**Figure 11.** χ_0^{-1} plotted against T/T_C over a wide temperature range for $T > T_C$. The dashed and continuous curves through the data points denote the least-squares fits based on equations (15) and (17), respectively.

Table 6. Parameter values for the LS fits, based on equation (17) of the text, to $\chi_0^{-1}(T)$ data taken over a wide temperature range.

Alloy conc.	Fit range (T/T_C)	T_C^+ (K)	γ	A_χ (10^{-3})	$\tilde{a}_\chi^+$	q_c (μ_B)	q_s (μ_B)	q_c/q_s
$y = 1$	1.0–1.43	209.60(8)	1.39(2)	4.5(3)	−2.0(4)	6.67(24)	1.34(2)	4.98(25)
$x = y = 0$	1.0–1.33	224.96(8)	1.39(2)	3.7(2)	−1.8(3)	6.25(22)	1.44(2)	4.34(20)
$x = 1$	1.0–1.17	256.67(10)	1.40(2)	2.9(2)	−2.5(4)	5.85(25)	1.52(2)	3.85(20)
$x = 2$	1.0–1.07	281.61(10)	1.39(2)	2.1(2)	−3.6(4)	5.13(30)	1.62(2)	3.17(20)
$x = 4$	1.0–1.35	327.98(10)	1.41(3)	1.5(2)	−1.5(4)	4.61(30)	1.79(2)	2.58(20)
$x = 6$	1.0–1.20	374.70(10)	1.42(3)	1.0(2)	−1.0(3)	3.92(30)	1.81(2)	2.17(20)
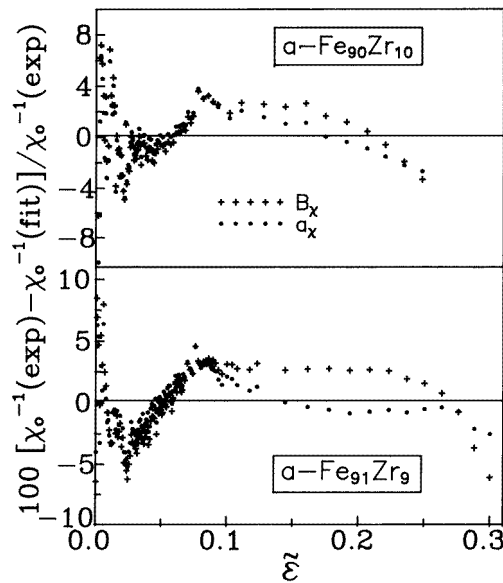
Figure 12. Percentage deviation of the $\chi_0^{-1}(T)$ data from the theoretical values corresponding to the least-squares fits based on equations (17) (●) and (18) (+).

straight line. The values of T_C, δ and D thus obtained are listed in table 7 along with values of δ calculated from the scaling relation $\delta = 1 + (\gamma/\beta)$ using the MAP values of β and γ as well as those of D calculated for the isotherm closest to T_C from (7). The values of T_C for all the alloy compositions determined by this method are in excellent agreement with those extracted using methods described earlier.

4. Discussion

4.1. Asymptotic and effective critical exponents and amplitudes

The present results demonstrate that the CTS analysis, which includes the nonanalytic correction terms, arising from nonlinear irrelevant scaling fields, yields accurate values for the *asymptotic* critical exponents and amplitudes that, in the ACR, are *independent* of the temperature range chosen for a CTS fit in the 'range-of-fit' analysis. On the other hand,
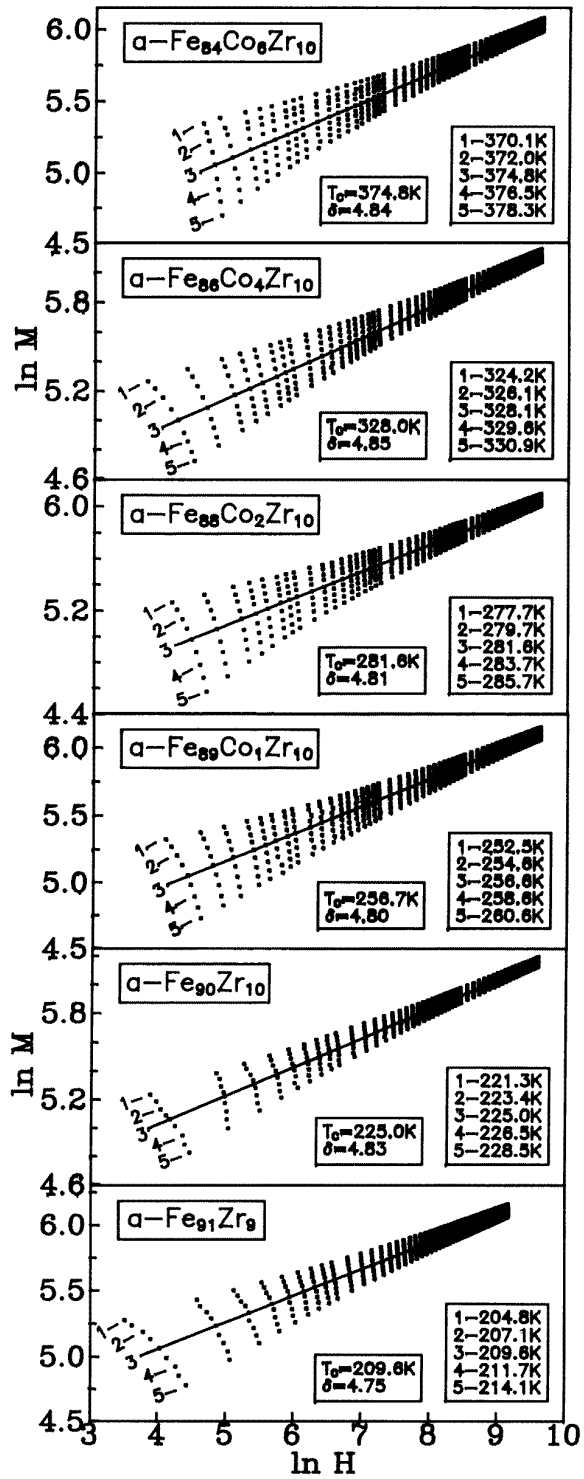
Figure 13. ln M–ln H isotherms at a few selected temperatures around T_C for a-Fe$_{90-x}$Co$_x$Zr$_{10}$ and a-Fe$_{90+y}$Zr$_{10-y}$ alloys.

Table 7. Parameter values for the critical isotherm. Values of δ and D within the square brackets are obtained by the MAP analysis (see text).

Alloy conc.	T_C (K)	δ	D (10^{-9} Oe$^{1-\delta}$)
$y = 1$	209.6(1)	4.75(5) [4.85(20)]	3.04(10) [3.60(20)]
$x = y = 0$	225.0(1)	4.83(4) [4.90(20)]	2.00(6) [0.81(30)]
$x = 1$	256.7(1)	4.80(4) [4.78(20)]	3.20(10) [3.07(25)]
$x = 2$	281.6(1)	4.81(5) [4.85(20)]	3.76(10) [3.43(25)]
$x = 4$	328.0(1)	4.85(5) [4.88(20)]	1.98(7) [1.45(25)]
$x = 6$	374.8(1)	4.84(5) [4.85(20)]	3.08(12) [2.11(30)]

the *effective* critical exponents and amplitudes obtained by using other methods of analysis (including KF and SPL) *depend* on the temperature range used and denote the *average* values over this temperature range. This observation is clearly brought out by the results presented in table 2. It is also noticed from this table that the results of KF and SPL analyses conform well with one another. Such an agreement is expected since both the methods are based on the same pure-power-law expressions (8) and (9) for $M(T, 0)$ and $\chi_0(T)$. The effective exponents β_{eff} and γ_{eff} as functions of temperature can be obtained from the KF relations (10) and (11) when they are put into the form [25, 26]

$$\beta_{eff}(T) = \frac{T - T_C}{|Y(T)|} = \frac{T_C \, \epsilon}{|Y(T)|} \qquad \gamma_{eff}(T) = \frac{(T - T_C)}{X(T)} = \frac{T_C \, \epsilon}{X(T)}. \tag{19}$$

The values of β_{eff} and γ_{eff} at different temperatures, thus obtained, are plotted as a function of ϵ in figures 14 and 15, respectively, within the ACR. The asymptotic and effective critical exponents for temperatures in close proximity to T_C (i.e., in the ACR) are related in accordance with the expressions [20, 22, 23, 29, 37]

$$\beta_{eff}(\epsilon) = \beta + a_{M_1}^- \Delta_1 |\epsilon|^{\Delta_1} + a_{M_2}^- \Delta_2 |\epsilon|^{\Delta_2} \tag{20}$$

and

$$\gamma_{eff}(\epsilon) = \gamma - a_{\chi_1}^+ \Delta_1 |\epsilon|^{\Delta_1} - a_{\chi_2}^+ \Delta_2 |\epsilon|^{\Delta_2}. \tag{21}$$

It is evident from these equations that over a finite temperature range around T_C, where the correction terms are significant, the effective exponents can appreciably differ from the asymptotic ones and that $\beta_{eff}(\epsilon)$ and $\gamma_{eff}(\epsilon)$ coincide with β and γ only in the limit $|\epsilon| \to 0$. This observation is clearly brought out by the data presented in figures 14 and 15 for the alloys in question. The continuous curves through the data points in these figures represent the theoretical fits to the β_{eff} [γ_{eff}] data based on (20) [(21)] obtained by keeping the CTS exponents (T_C) fixed at their theoretical values $\Delta_1 = 0.11$ and $\Delta_2 = 0.55$ (at the KF value obtained in the range $|\epsilon| \lesssim 0.01$) and treating β, $a_{M_1}^-$ and $a_{M_2}^-$ [γ, $a_{\chi_1}^+$ and $a_{\chi_2}^+$] as free fitting parameters. The values of these parameters determined in this way serve as a cross-check for those deduced from the CTS analysis of $M(T, 0)$ and $\chi_0(T)$ data (tables 3 and 4) in the ACR because the above analysis involves *three* fitting parameters as against *five* in the CTS analysis. Therefore, it is gratifying to note that the two analyses yield the

same parameter values. Moreover, the necessity of including the (nonanalytic) confluent singularity corrections in the analysis is evident from the functional dependences of β_{eff} and γ_{eff} on ϵ depicted in figures 14 and 15 when it is recognized that the exponents β_{eff} and γ_{eff} should be *independent* of temperature if such correction terms are not important. Another interesting feature presented by the data shown in these figures is that both β_{eff} and γ_{eff} *increase* with increasing $|\epsilon|$ for the alloys investigated as contrasted with a monotonic decreasing trend with increasing $|\epsilon|$ exhibited by these effective exponents in the ACR in many amorphous 3d transition metal–metalloid ferromagnetic alloys as well as crystalline elemental ferromagnets [20, 22, 23, 25, 37]. Consistent with this variation of $\beta_{eff}(\epsilon)$ and $\gamma_{eff}(\epsilon)$, the sign of the CTS amplitudes (*positive* for $a_{M_2}^-$ and *negative* for $a_{M_1}^-$, $a_{\chi_1}^+$ and $a_{\chi_2}^+$, tables 3 and 4) in the present case is exactly opposite to that previously found in the ferromagnetic systems mentioned above. However, the overall behaviour of $\gamma_{eff}(\epsilon)$ in a larger temperature range, i.e., from T_C to $T_{\max}$ (the maximum temperature covered in the present experiments), shown in figure 16, for the present alloys is similar to that observed earlier in a number of disordered systems [22, 23, 26, 27, 32, 33]. The continuous curves in figure 16 represent the CTS fits to the $\gamma_{eff}(\epsilon)$ data based on (21) in the ACR, as described above. It is evident from these figures that for temperatures outside the ACR, i.e., for $\epsilon > \epsilon_{co}^+$, γ_{eff} increases rapidly and goes through a peak (peak value γ_{eff}^p) at ϵ_p and, as the Co concentration is increased, $\epsilon_{co}^+(\epsilon_p)$ exhibits an increasing (decreasing) trend (i.e., shifts to higher (lower) temperatures) while γ_{eff}^p slowly diminishes in value.

Table 8 tests the validity of the Widom scaling relation, $\beta\delta = \beta + \gamma$, for the investigated alloys besides comparing the experimentally determined values of asymptotic exponents β, γ and δ with the corresponding theoretical estimates yielded by three-dimensional (3D) Heisenberg, Ising and XY models for ordered or quenched random-exchange spin systems [13–16, 18, 26]. The values for the amplitude ratios Dm_0^δ/h_0, $m_0/M(0,0)$ and $\mu_0 h_0/k_B T_C$ (μ_0 is the magnetic moment per alloy atom at 0 K) calculated using the determined values of asymptotic critical amplitudes are listed in table 9 along with the corresponding theoretical estimates [23, 26, 38, 39]. The main observations, based on the data presented in tables 8 and 9, are (i) the values for the asymptotic critical exponents and the universal amplitude ratios Dm_0^δ/h_0 and $a_{M_2}^-/a_{\chi_2}^+$ are *composition independent* (within the error limits) and conform very well with the theoretical estimates [40] for the pure (ordered) spin system with $d = n = 3$, (ii) the ratio $a_{M_1}^-/a_{\chi_1}^+$, which involves the leading CTS amplitudes that arise only in the presence of quenched disorder, like the ratio $a_M^-/a_\chi^+ (= a_{M_2}^-/a_{\chi_2}^+)$ involving the CTS amplitudes which are also present in the case of ordered systems, turns out to be *composition independent* (and hence could be universal as well), (iii) the Widom scaling relation is satisfied to a far greater accuracy by the asymptotic critical exponents than by the effective ones, (iv) the agreement between theory and experiment is much better for the asymptotic exponents than for the effective counterparts and (v) while the discrepancy between experimental and theoretical values of the ratio $m_0/M(0,0)$ is small, the ratio $\mu_0 h_0/k_B T_C$ is at least one order of magnitude lower than the theoretical estimate of 1.58 for a 3D Heisenberg ferromagnet.

The finding that the values of asymptotic critical exponents for the a-$Fe_{90-x}Co_xZr_{10}$ and a-$Fe_{90+y}Zr_{10-y}$ alloys are the same as those of an isotropic 3D Heisenberg ferromagnet refutes the earlier claims [2, 3], based on the single-power-law analysis, that for the same alloys critical exponents β and γ have anomalously large values. The results of the present investigation make it clear that such unphysically large exponent values as well as the spread in the reported exponent values are an artifact [41] of the analysis carried out on the bulk magnetization data taken outside the critical region since, even in the ACR, $\beta_{eff}(\epsilon)$ and $\gamma_{eff}(\epsilon)$ depend on temperature (figures 14 and 15) and possess much larger values
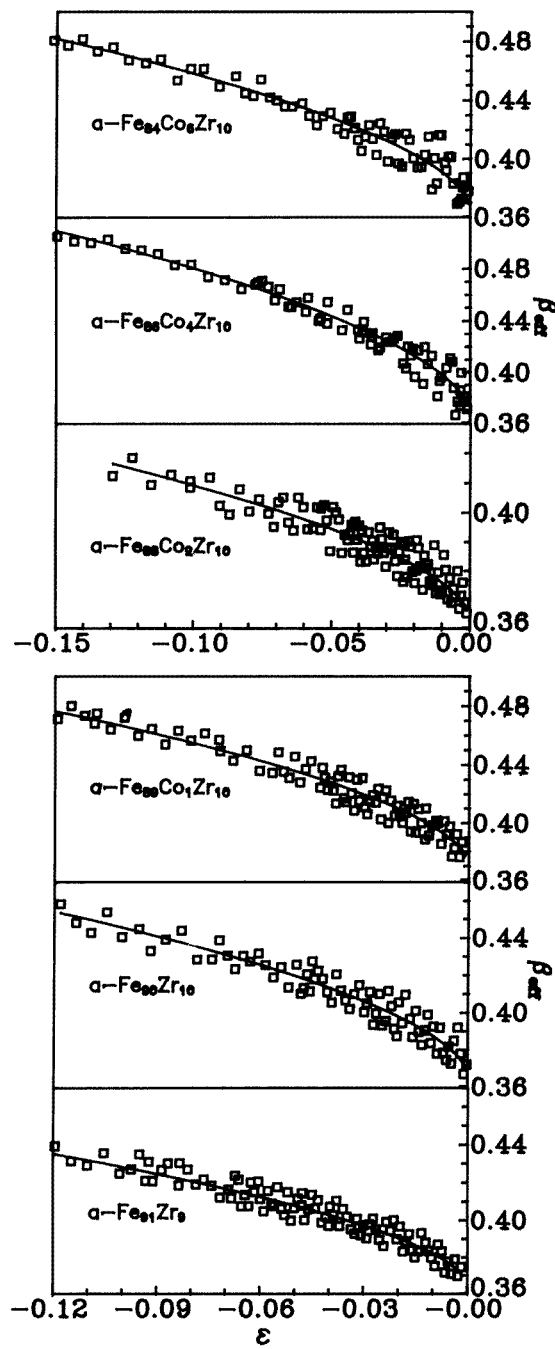
Figure 14. β_{eff} plotted against ϵ in the ACR. The continuous curves denote the least-squares fits based on equation (20). The typical uncertainty limits for the $\beta_{eff}(\epsilon)$ data are ± 0.01.
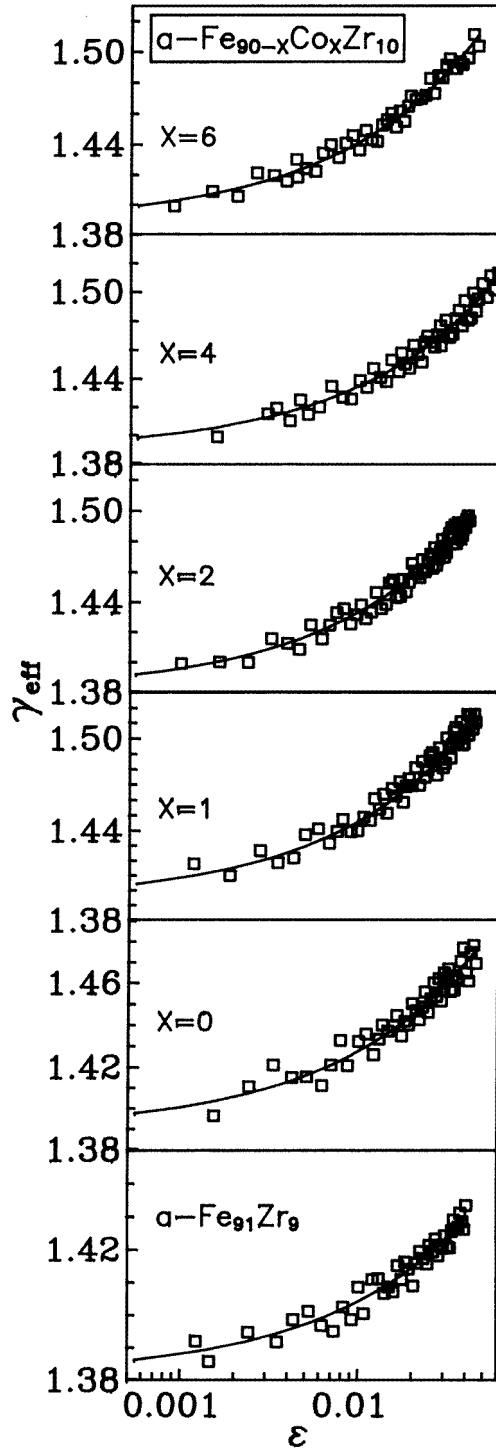
Figure 15. γ_{eff} plotted against ϵ in the ACR. The continuous curves represent the least-squares fits based on equation (21). The typical uncertainty limits for the $\gamma_{eff}(\epsilon)$ data are ± 0.01.
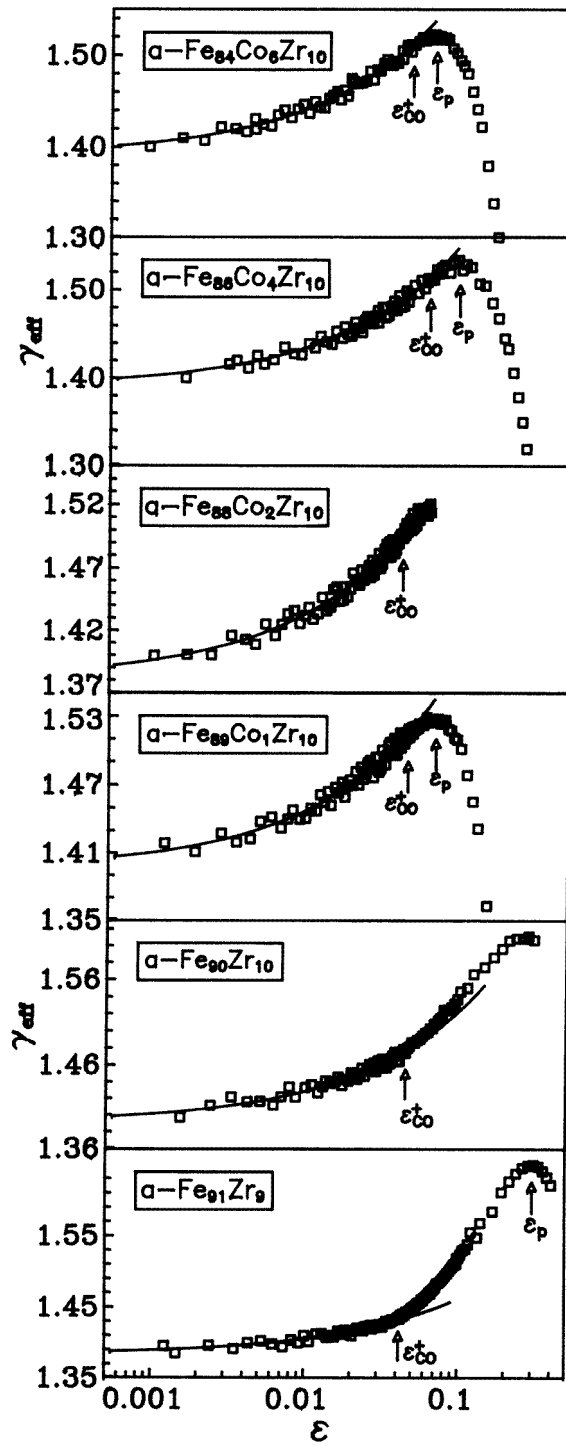
Figure 16. The variation of γ_{eff} with ϵ over a wide temperature range for $T > T_C$. The solid curves through the data points denote the least-squares fits, obtained in the ACR, based on equation (21). The typical uncertainty limits for the $\gamma_{eff}(\epsilon)$ data are ± 0.01.

Table 8. A comparison between theory and experiment: asymptotic and effective critical exponents, and validity of the Widom scaling equality. CTS, correction to scaling; HM, Heisenberg model; IM$_p$, pure (ordered) Ising model; IM$_r$, quenched random Ising model; KF, Kouvel–Fisher; MFT, mean-field theory.

Alloy conc.	Analysis	β	γ	δ	$\beta+\gamma$	$\beta\delta$
$y=1$	CTS	0.366(4)	1.383(4)	4.75(5)	1.749(8)	1.739(38)
	KF	0.382(15)	1.400(20)		1.782(35)	1.807(90)
$x=y=0$	CTS	0.360(5)	1.390(5)	4.83(4)	1.750(10)	1.739(39)
	KF	0.382(15)	1.405(20)		1.787(35)	1.845(88)
$x=1$	CTS	0.368(6)	1.385(5)	4.80(4)	1.753(11)	1.766(43)
	KF	0.384(15)	1.416(25)		1.800(40)	1.836(87)
$x=2$	CTS	0.363(5)	1.389(6)	4.81(5)	1.752(11)	1.746(42)
	KF	0.381(15)	1.388(20)		1.769(35)	1.825(90)
$x=4$	CTS	0.365(6)	1.383(7)	4.85(5)	1.748(13)	1.770(48)
	KF	0.386(15)	1.407(20)		1.793(35)	1.872(92)
$x=6$	CTS	0.370(5)	1.386(6)	4.84(5)	1.756(11)	1.791(43)
	KF	0.390(15)	1.402(20)		1.792(35)	1.888(93)
3D HM[a]		0.365(3)	1.386(4)	4.80(4)	1.751(7)	1.752(30)
3D IM$_p$[a]		0.325(2)	1.241(2)	4.82(3)	1.566(4)	1.567(20)
3D IM$_r$[a]		0.349(2)	1.336(2)	4.83(3)	1.685(4)	1.686(20)
3D XY[a]		0.345(2)	1.316(3)	4.81(3)	1.661(5)	1.660(20)
MFT		0.500	1.000	3.00	1.500	1.500

[a] [16, 18, 23, 26].

Table 9. A comparison between theory and experiment: amplitude ratios. Abbreviations have the same meaning as in table 8.

Conc. (y/x)	h_0 (10^5 Oe)	Dm_0^δ/h_0	$a_{M_1}^-/a_{\chi 1}^+$	$a_{M_2}^-/a_{\chi 2}^+$	$M(0,0)$ (G)	$m_0/M(0,0)$	$\mu_0 h_0/k_B T_C$	μ_{eff} (μ_B)	c (%)
$y=1$	1.4(1)	1.30(60)	1.0(7)	$-1.0(4)$	965(25)	0.82(4)	0.060(5)	35.2(25)	4(1)
$x=y=0$	1.9(2)	1.32(65)	1.0(5)	$-1.1(4)$	1041(30)	0.79(5)	0.082(7)	27.7(22)	5(1)
$x=1$	2.6(2)	1.34(65)	0.8(4)	$-0.8(3)$	1100(35)	0.76(4)	0.104(11)	23.0(21)	7(1)
$x=2$	4.0(3)	1.30(65)	0.8(4)	$-0.7(2)$	1170(25)	0.75(4)	0.154(14)	16.7(13)	10(1)
$x=4$	5.3(4)	1.33(85)	1.2(5)	$-0.8(3)$	1296(20)	0.77(4)	0.194(26)	14.7(18)	12(1)
$x=6$	6.0(5)	1.33(95)	1.0(5)	$-0.7(3)$	1305(30)	0.83(4)	0.195(31)	14.8(23)	12(1)
3D HM[a]		1.33(1)				1.37(7)	1.58		
3D IM$_p$[a]		1.81		0.90(21)[b]		1.49	1.52		
MFT[a]		1.00				1.73	1.73		

[a] [23, 26, 38, 39].

[b] [38, 39].

for $\epsilon > \epsilon_{co}^+$ (see, e.g., figure 16). The observation that the values of asymptotic critical exponents and universal amplitude ratios for the investigated amorphous alloys exactly coincide with the 3D Heisenberg values (observation (i)) vindicates the Harris criterion [19] and testifies to the correctness of the RG predictions [13–16] that the critical behaviour of a quenched random-exchange $d = 3$ Heisenberg ferromagnet is the same as that of the pure (ordered) $d = n = 3$ spin system. Moreover, this observation permits us to conclude that the systems studied in this work belong to the $d = n = 3$ universality class. That these glassy systems are not the experimental realizations of the quenched random-anisotropy model (RAM) is asserted by the fact that none of the theoretical predictions [42] based on

RAM, i.e., the Harris criterion does not apply and, depending on particular assumptions, the system exhibits (a) a first-order phase transition, (b) crossover to a new fixed point or (c) two transitions, the first to a state of zero magnetization and infinite susceptibility, the second to a state of finite susceptibility, is borne out by the present experimental results. Validity of the Widom scaling relation for the alloys in question (observation (iii)) demands that the $M(T, H)$ data taken in the critical region must satisfy the scaling equation of state for a second-order phase transition, i.e., SES I (4) or even SES II (5). That this is indeed the case for a-$Fe_{90-x}Co_xZr_{10}$ and a-$Fe_{90+y}Zr_{10-y}$ alloys is evident from figures 1 and 2. The physical implication of the significantly lower values of the ratio $\mu_0 h_0 / k_B T_C$ than that expected for a 3D nearest-neighbour (NN) Heisenberg ferromagnet is as follows. Since h_0 is presumably an *effective* exchange interaction field, the product of h_0 and an *average effective* elementary moment (μ_{eff}) involved in the FM–PM phase transition, i.e., the effective exchange energy $\mu_{eff} h_0$, is expected to equal the thermal energy $k_B T_C$ at T_C. Evidently, this is not the case for the alloys in question unless μ_{eff} takes on values that are much larger than μ_0. Now that the critical exponents possess the 3D Heisenberg values for the presently investigated alloys, the ratio $\mu_{eff} h_0 / k_B T_C$ is also expected to equal the 3D Heisenberg estimate of 1.58. This is possible only when μ_{eff} assumes values given in table 9. Moreover, if the concentration of such effective moments is c, $c = \mu_0 / \mu_{eff}$. The values of c calculated in this way, included in table 9, indicate that only a small fraction of moments actually participates in the FM–PM phase transition and this fraction increases with increasing Co concentration (x).

These results find a straightforward but qualitative explanation [4, 22, 23, 26, 32] in terms of the infinite ferromagnetic (FM) matrix plus finite FM spin clusters model (the details of this model are given in our earlier reports [4, 26, 43]), as is evident from the remarks made below. Within the framework of this model, even at low temperatures ($T \ll T_C$), the ferromagnetic coupling between the spins that constitute the finite clusters is much *stronger* than that between the spins of the FM matrix. As the temperature is increased towards T_C, the exchange interaction between the spins in the FM matrix weakens whereas the FM coupling between the spins within the finite clusters is still relatively strong so that the spins of finite clusters increasingly polarize the FM matrix spins and hence these clusters grow in size at the expense of the FM matrix. Consequently, the number of spins in the FM matrix decreases rapidly as $T \to T_C$, so much so that only a small fraction of spins participates in the FM–PM phase transition at T_C. In Co containing alloys, the Fe–Co and Co–Co exchange interactions are ferromagnetic and much stronger than the Fe–Fe exchange coupling, with the result that a progressive replacement of Fe by Co in a-$Fe_{90-x}Co_xZr_{10}$ alloys gradually suppresses the competing interactions in the frustration zones. This, in turn, leads to breaking up of finite spin clusters into smaller ones and merging of some of them with the infinite FM matrix. Hence the effect of increasing Co concentration in the a-$Fe_{90-x}Co_xZr_{10}$ alloy series is to (i) decrease the size as well as number of finite spin clusters, (ii) increase the number of spins in the infinite FM matrix and (iii) make the ferromagnetic coupling between the spins in the FM matrix stronger (hence increase T_C). This implies that the higher the Co concentration, the larger is the number of spins available in the FM matrix to start with at low temperatures and the greater is the number of spins left behind at T_C by the temperature-induced growth of finite spin clusters. In other words, consistent with the present observation, the fraction of spins, c, participating in the FM–PM transition at T_C increases with increasing Co concentration. Moreover, since the spin–spin correlation length, $\xi(T)$, diverges [44] at T_C, the presence of finite clusters is not felt at all for temperatures close to T_C and as such amorphous and crystalline ferromagnets exhibit the same critical behaviour in the ACR. As the temperature is increased beyond

T_C, $\xi(T)$ decreases and a temperature ϵ_{co}^+ is reached at which $\xi(T)$ is equal to the caliper dimension of the largest spin cluster. The magnetic inhomogeneity in the spin system is now no longer averaged out and γ_{eff} begins to increase and attains a peak value γ_{eff}^p at ϵ_p when $\xi(T)$ is comparable to the linear dimension of the smallest cluster. For $\epsilon > \epsilon_p$, the clusters shrink in size at a much faster rate than that at which $\xi(T)$ decreases with increasing temperature and hence γ_{eff} decreases towards the mean-field value. Furthermore, as the Co concentration is increased, the size of clusters as well as their number decreases and hence $\xi(T)$ becomes comparable to the size of the largest (smallest) cluster at a larger value of the temperature $\epsilon_{co}^+(\epsilon_p)$ whereas γ_{eff}^p decreases because of the lower average size and narrower size distribution of the spin clusters for higher Co concentrations.

A recent claim [45] that the magnetic ordering behaviour of a-$Fe_{90+y}TM_{10-y}$ (TM = Zr, Hf, Sc) alloys for temperatures in the range $0 \lesssim T \lesssim T^*$ ($T^* > T_C$ or T_{xy}, the transverse spin freezing temperature) can be completely understood in terms of the *homogeneous* transverse spin freezing (TSF) model prompted us to explore the possibility of explaining the above observations in the light of this model. Considering that this model is based on a bond-frustrated 3D Heisenberg model [46], critical exponents and universal amplitude ratios are expected to possess 3D NN Heisenberg values. Moreover, in the TSF model, a progressive substitution of Fe by Co in a-$Fe_{90-x}Co_xZr_{10}$ alloys amounts to a random replacement of antiferromagnetic Fe–Fe exchange bonds by ferromagnetic Co–Fe and Co–Co exchange bonds and hence to an enhancement in the value of T_C. Both the above inferences conform well with our results. Now that the TSF model asserts that T_C marks the temperature at which a transition occurs from the paramagnetic state to a state with *homogeneous* long-range ferromagnetic ordering, the presently studied spin systems should behave exactly the same way as crystalline (ordered) ferromagnets do so far as the behaviour in the critical region and at temperatures well above T_C is concerned. The observations such as (i) only a small fraction of moments participating in the FM–PM transition and this fraction increasing with Co concentration, (ii) a peak in $\gamma_{eff}(\epsilon)$ at ϵ_p and (iii) the dependence of ϵ_p, γ_{eff}^p and ϵ_{co}^+ on Co concentration, *specific* to amorphous ferromagnets only, are in direct *contradiction* with the above predictions of the TSF model.

4.2. Nonlinear scaling behaviour

Elaborate analysis of the $M(T, 0)$ and $\chi_0(T)$ data in terms of the expressions predicted by the nonlinear scaling theory [36] reveals that (i) the *nonanalytic* CTS terms essentially control the temperature dependence of $M(T, 0)$ and $\chi_0(T)$ for temperatures close to T_C, (ii) in the ACR, nonlinear scaling theory yields exactly the same results as its linear counterpart does and (iii) the *analytic* corrections become important for temperatures outside the ACR. Since the expression that includes a single leading analytic correction term in nonlinear variable $\tilde{\epsilon}$, i.e., (17), adequately describes the $\chi_0(T)$ data over a wide temperature range above T_C for the investigated alloys and thereby permits an unambiguous determination of the magnetic moment per alloy atom in the paramagnetic state, q_c, (17) may be termed as the generalized Curie–Weiss law [36]. The Curie constant $C = A_\chi T_C$ is related to the effective paramagnetic moment (p_{eff}) as $p_{eff} = 2.828\sqrt{CA/\rho}$, where A and ρ are the atomic weight and density, respectively. p_{eff}, in turn, is related to q_c as $p_{eff}^2 = q_c(q_c + 2)$. The values of q_c, computed from these relations using the A_χ and T_C values listed in table 6, and those of the ratio q_c/q_s, where $q_s(\equiv \mu_0)$ is the magnetic moment per alloy atom at 0 K, are included in table 6. For all the amorphous alloys in question, the ratio $q_c/q_s \gg 1$ and its values for different compositions when plotted against T_C^{-1} or $T_C^{-2/3}$ fall on a straight line as shown in figure 17. According to the criteria proposed by Rhodes

and Wohlfarth [47] and Moriya [47] for weak itinerant ferromagnetism, the observations $q_c/q_s \gg 1$ and $q_c/q_s \propto T_C^{-1}$ or $q_c/q_s \propto T_C^{-2/3}$ imply that the amorphous alloys investigated are *weak* itinerant ferromagnets. Note that our results are unable to make a clear-cut distinction between the two criteria because the range of T_C values covered in the present experiments is not wide enough. The observation that these weak itinerant ferromagnets behave like 3D NN Heisenberg ferromagnets in the critical region, when considered in conjunction with the result of the renormalization group calculations [48] that for a *d*-dimensional spin system with an *isotropic n*-component order parameter and *long-range* attractive interactions decaying as $1/r^{d+\sigma}(\sigma > 0)$, critical exponents assume their *short-range* values for all *d* if $\sigma > 2$, asserts that the magnetic moments in the systems investigated interact with one another through a *long-range* interaction which *decays faster* than $1/r^5$ with the intermoment spacing, *r*. The above considerations strongly indicate that it is the itinerant-electron model and *not* the localized-electron (Heisenberg) model, on which the TSF model [45] is based, that forms the *correct* description of magnetism in the glassy materials of interest in this work.
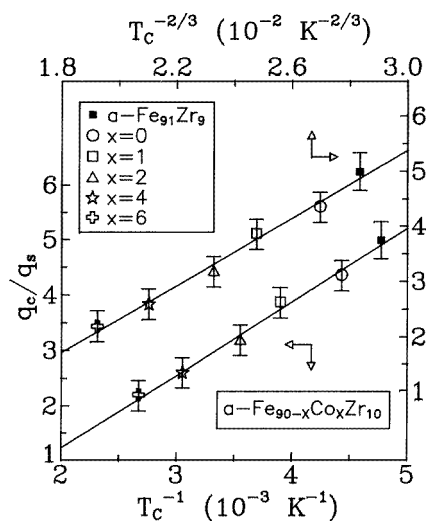

Figure 17. q_c/q_s against T_C^{-1} and q_c/q_s against $T_C^{-2/3}$ plots. The solid line denotes the least-squares straight-line fit to the data.

A cursory glance at the MAPs depicted in figures 3 and 9 suffices to reveal that the slope of the MAP isotherms decreases continuously with increasing temperature. This feature of MAP is characteristic [4, 5, 22, 23, 26, 27, 32, 33, 36, 37] of both crystalline and amorphous ferromagnets. The Arrott–Noakes equation of state in linear variables ϵ and H (i.e., (6)) cannot account for this variation in the slope of MAP isotherms since the coefficients a' and b' in (6) are temperature independent. By contrast, the magnetic equation of state in nonlinear variables $\tilde{\epsilon}$ and $\tilde{h}$ of the form

$$M^{1/\beta} = a(-\tilde{\epsilon}) + bt^{-1/\gamma}(H/M)^{1/\gamma} \tag{22}$$

with

$$a \simeq \tilde{A}_M[1 + \tilde{a}_{M_1}^-|\tilde{\epsilon}|^{\Delta_1} + \tilde{a}_{M_2}^-|\tilde{\epsilon}|^{\Delta_2}] \tag{23}$$

and

$$b \simeq \tilde{A}[1 + \tilde{a}_1|\tilde{\epsilon}|^{\Delta_1} + \tilde{a}_2|\tilde{\epsilon}|^{\Delta_2}] \tag{24}$$

or

$$a = [B'_M(1 + \tilde{a}_M\tilde{\epsilon})]^{1/\beta} \simeq A_M[1 + a_M\tilde{\epsilon}] \tag{25}$$

and

$$b = [B_M(1 + \tilde{a}_M\tilde{\epsilon})]^{1/\beta}[A_\chi(1 + \tilde{a}_\chi\tilde{\epsilon})]^{1/\gamma} \simeq A[1 + \tilde{a}\tilde{\epsilon}] \tag{26}$$

yielded by the NL scaling theory [36], predicts the temperature dependence of the MAP intercept ($= a(-\tilde{\epsilon})$) and slope ($= bt^{-1/\gamma}$) of the type given by (23) or (25) and (24) or (26), respectively. Note that (23) and (24) ((25) and (26)) contain nonanalytic (analytic) correction terms alone but the NL theory predicts the expressions that combine both types of correction. However, to facilitate comparison with experiment, it is convenient to separate correction terms that become important in different temperature ranges. Encouraged by the accurate predictions that the nonlinear scaling theory makes about the temperature dependence of $M(T, 0)$ and $\chi_0(T)$ over a wide temperature range, which embraces the critical region, a detailed analysis of the observed temperature variation of the MAP intercept and slope in terms of (22)–(26) was undertaken. The main outcome of this exercise is that the observed temperature variation of slope and intercept (on the MAP ordinate) is closely reproduced (figure 18) by the relations, slope $(T) = bt^{-1/\gamma}$ and intercept (T) [$\equiv M^{1/\beta}(T, 0)$] $= a(-\tilde{\epsilon})$, respectively, for temperatures in the immediate vicinity of T_C (over a much wider temperature range) with the expressions for the coefficients a and b given by (23) and (24) [dashed curves] ((25) and (26) [continuous curves]). Such an agreement between the theory and experiment is representative of all the compositions studied. This implies that the nonanalytic correction terms dominate over the analytic ones for temperatures close to T_C whereas the reverse is true for temperatures away from T_C. This result is consistent with the similar observation made above in the case of $M(T, 0)$ and $\chi_0(T)$. Furthermore, when the intercept data for $T \leqslant T_C$ only are used in the analysis, the term $a(-\tilde{\epsilon})$ with the coefficient a given by either (23) or (25) provides the best fit with the choice of parameters and temperature range that is exactly the same as that for the fit to $M(T, 0)$ data based on (14) or (16). This result is not surprising when it is realized that the intercepts for $T \leqslant T_C$ are nothing but $M(T, 0)$ expressed as $[M(T, 0)]^{1/\beta}$.

Note that in the limit $|\tilde{\epsilon}| \to 0$ (or equivalently $t \to 1$), (22) reduces to the Arrott–Noakes (AN) scaling equation of state (SES) (6), as the coefficients a and b assume their limiting *temperature-independent* values $\tilde{A}_M$ and $\tilde{A}$, respectively. Thus, the AN SES represents a special case of the more general SES given by (22) and is strictly valid only for temperatures extremely close to T_C, i.e., in the limit $|\epsilon|$ or $|\tilde{\epsilon}| \to 0$, since it is based on the asymptotic power laws described by (1) and (2). At this stage, it should be emphasized that the customary practice of choosing the exponents β and γ such that MAP isotherms over a broad temperature range around T_C are straight and *parallel* to one another in accordance with the AN SES (6) is bound to yield incorrect functional dependences of spontaneous magnetization, M_S, and initial susceptibility, χ_0, on temperature, especially in the critical region. This is so because, in such a case, *temperature-dependent effective* critical exponents β_{eff} and γ_{eff}, defined by (8) and (9), replace *asymptotic* critical exponents β and γ in (6) and $\beta_{eff}(\epsilon)$ and $\gamma_{eff}(\epsilon)$ (figures 14 and 15), in turn, decide the variations of M_S and χ_0 with temperature. Alternatively, temperature dependences of M_S or χ_0 obtained from such MAPs, even in a temperature region that is common to MAPs constructed from $M(T, H)$ data taken in different temperature ranges around T_C, vary from MAP to MAP because they are basically controlled by effective exponents whose values depend on the temperature range chosen for the MAP. This problem is effectively tackled by using the asymptotic values of the critical exponents β and γ (obtained by the SES III method) in constructing
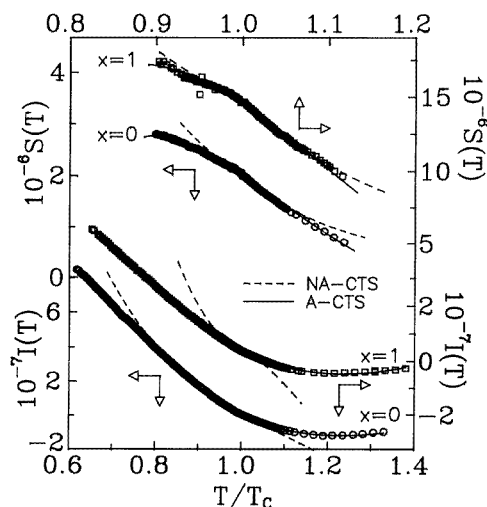
Figure 18. Variation of slope $\equiv S(T) = bt^{-1/\gamma}$ and intercept (on the ordinate) $\equiv I(T) = a(-\tilde{\epsilon})$ of the linear MAP isotherms over a wide temperature range around T_C. Dashed and continuous curves represent the least-squares fits to the data with the coefficients a and b given by equations (23), (24) and (25), (26), respectively.

the MAPs over a wide range of temperatures because, in this case, the generalized magnetic equation of state (22) (which includes the corrections to asymptotic power laws arising from nonlinear irrelevant and relevant scaling fields and hence adequately describes the magnetization behaviour over wide ranges of field, particularly in the high-field region, and temperature, as evident from the data presented in figures 9 and 18) and *not* the AN SES (6) forms the basis for MAPs.

5. Conclusions

The main conclusions regarding the thermal critical behaviour of a-Fe$_{90-x}$Co$_x$Zr$_{10}$ and a-Fe$_{90+y}$Zr$_{10-y}$ alloys that can be drawn from the results of the bulk magnetization measurements on these systems over a wide temperature range, which embraces the critical region, are as follows.

(i) The asymptotic critical exponents and the universal amplitude ratios Dm_0^δ/h_0 and $a_{M_2}^-/a_{\chi_2}^+$, are in very good agreement with the corresponding theoretical estimates for the pure (ordered) spin system with $d = n = 3$. Such an agreement vindicates the famous Harris criterion.

(ii) Consistent with the result that Widom scaling equality is satisfied to a very high degree of accuracy, the magnetization data obey the scaling equation of state valid for the second-order phase transition.

(iii) The fraction of spins that actually participates in the FM–PM phase transition in the amorphous alloys in question is small and increases with increasing Co concentration.

(iv) Nonanalytic correction terms, arising from nonlinear irrelevant scaling fields, dominate over the analytic ones, originating from nonlinear relevant scaling fields, in the asymptotic critical region, but the reverse is true for temperatures outside the ACR.

(v) The magnetic equation of state in linear scaling variables, valid for a second-order

phase transition, describes the magnetization data for temperatures close to T_C, whereas its counterpart in nonlinear scaling variables properly accounts for the observed $M(T, H)$ behaviour in a much wider temperature range around T_C.

(vi) $\chi_0(T)$ follows the generalized Curie–Weiss law (17) from T_C to $\sim 1.5T_C$ and thereby makes an unambiguous determination of the atomic moment in the paramagnetic state possible.

(vii) All the investigated amorphous alloys are *weak* itinerant ferromagnets.

(viii) The infinite 3D FM matrix plus finite FM spin cluster model provides a simple but qualitative explanation for all the diverse aspects of the present results including the temperature variations of γ_{eff}^{KF}.

References

[1] Hiroyoshi H, Fukamichi K, Hoshi A and Nakagawa Y 1983 *High Field Magnetism* ed M Date (Amsterdam: North-Holland) p 113
[2] Yamamoto H, Onodera H, Hosoyama K, Masumoto T and Yamauchi H 1983 *J. Magn. Magn. Mater.* **31–34** 1579
   Yamauchi H, Onodera H and Yamamoto H 1984 *J. Phys. Soc. Japan* **53** 747
[3] Winschuh K and Rosenberg M 1987 *J. Appl. Phys.* **61** 4401
[4] Kaul S N 1988 *J. Phys. F: Met. Phys.* **18** 2089
[5] Reisser R, Fähnle M and Kronmüller H 1988 *J. Magn. Magn. Mater.* **75** 45
   Reisser R, Seeger M, Fähnle M and Kronmüller H 1992 *J. Magn. Magn. Mater.* **110** 32
[6] Kaul S N, Hofmann A and Kronmüller H 1986 *J. Phys. F: Met. Phys.* **16** 365
   Kaul S N 1987 *J. Appl. Phys.* **61** 451
[7] Ma H, Kunkel H P and Williams G 1991 *J. Phys.: Condens. Matter* **3** 5563
[8] Kaul S N and Mohan Ch V 1991 *J. Phys.: Condens. Matter* **3** 2703
[9] Kaul S N and Babu P D 1992 *Phys. Rev.* B **45** 295
   Siruguri V and Kaul S N 1996 *J. Phys.: Condens. Matter* **8** 4567
[10] Pureur P, Schreiner W H, Kunzler J V, Ryan D H and Coey J M D 1988 *Solid State Commun.* **65** 163
[11] Mohan Ch V, Babu P D, Sambasiva Rao M, Lucinski T and Kaul S N 1993 *Proc. Int. Conf. on Disordered Materials (Poonam, 1993)* ed S K Srivastava p 158
[12] Rhyne J J, Erwin R W, Fernandez-Baca J A and Fish G E 1988 *J. Appl. Phys.* **63** 4080
   Rhyne J J and Fish G E 1985 *J. Appl. Phys.* **57** 3407
[13] Lubensky T C 1975 *Phys. Rev.* B **11** 3573
   Khmelńitzki D E 1975 *Zh. Eksp. Teor. Fiz.* **68** 1960 (Engl. transl. *Sov. Phys.–JETP* **41** (1976) 981)
[14] Grinstein G and Luther A 1976 *Phys. Rev.* B **13** 1329
   Aharony A 1976 *Phys. Rev.* B **13** 2092
[15] Weinrib A and Halperin B I 1983 *Phys. Rev.* B **27** 413
[16] Jug G 1983 *Phys. Rev.* B **27** 609
[17] Heuer H O and Wagner D 1989 *Phys. Rev.* B **40** 2502
[18] Le Guillou J C and Zinn-Justin J 1980 *Phys. Rev.* B **21** 3976
[19] Harris A B 1974 *J. Phys. C: Solid State Phys.* **7** 1671
[20] Kaul S N 1988 *Phys. Rev.* B **38** 9178
[21] Kaul S N and Sambasiva Rao M 1991 *Phys. Rev.* B **43** 11240
[22] Kaul S N and Mohan Ch V 1994 *Phys. Rev.* B **50** 6157
[23] Kaul S N and Sambasiva Rao M 1994 *J. Phys.: Condens. Matter* **6** 7403
   Sambasiva Rao M and Kaul S N 1995 *J. Magn. Magn. Mater.* **147** 149
[24] Ryan D H, Coey J M D, Batalla E, Altounian Z and Ström-Olsen J O 1987 *Phys. Rev.* B **35** 8630
[25] Kouvel J S and Fisher M E 1964 *Phys. Rev.* **136A** 1626
[26] Kaul S N 1985 *J. Magn. Magn. Mater.* **53** 5 and reference cited therein
   Kaul S N 1984 *IEEE Trans. Magn.* **MAG-20** 1290
[27] Fähnle M, Kellner W U and Kronmüller H 1987 *Phys. Rev.* B **35** 3640
   Kellner W U, Fähnle M, Kronmüller H and Kaul S N 1987 *Phys. Status Solidi* b **144** 397
[28] Arrott A and Noakes J E 1967 *Phys. Rev. Lett.* **19** 786
[29] Aharony A and Ahlers G 1980 *Phys. Rev. Lett.* **44** 782
[30] Aharony A and Fisher M E 1983 *Phys. Rev.* B **27** 4394

[31] Aharony A 1976 *Phase Transitions and Critical Phenomena* vol 6, ed C Domb and M S Green (New York: Academic) p 357
[32] Kaul S N, Kellner W-U and Kronmüller H 1987 *Key. Eng. Mater.* **13–15** 669
[33] Reisser R, Fähnle M and Kronmüller H 1991 *J. Magn. Magn. Mater.* **97** 83
[34] Hargraves P and Dunlap R A 1988 *J. Phys. F: Met. Phys.* **18** 533
     Hargraves P and Dunlap R A 1988 *J. Magn. Magn. Mater.* **75** 378
[35] Souletie J and Tholence J L 1983 *Solid State Commun.* **48** 407
[36] Kaul S N 1994 *Phase Transitions* **47** 23
[37] Seeger M, Kaul S N, Kronmüller H and Reisser R 1995 *Phys. Rev.* B **51** 12 585
[38] Privman V, Hohenberg P C and Aharony A 1991 *Phase Transitions and Critical Phenomena* vol 14, ed C Domb and J L Lebowitz (New York: Academic) p 1
[39] Bagnuls C, Breviller C, Meiron D I and Nickel B G 1987 *Phys. Rev.* B **35** 3585
[40] No theoretical estimates for the universal amplitude ratio a_M^-/a_χ^+ for the ordered $d = n = 3$ spin system are presently available
[41] Babu P D and Kaul S N 1995 *Phys. Rev.* B **52** 10 637
[42] Mukamel D and Grinstein G 1982 *Phys. Rev.* B **25** 381
     Fisch R 1990 *Phys. Rev.* B **41** 11705
[43] Kaul S N 1991 *J. Phys.: Condens. Matter* **3** 4027
     Kaul S N, Siruguri V and Chandra G 1992 *Phys. Rev.* B **45** 12 343
[44] Fernández Barquin L, Gómez Sal J, Kaul S N, Barandiarán J M, Gorria P, Pedersen J S and Heenan R 1996 *J. Appl. Phys.* **79** 5146
[45] Ren H and Ryan D H 1995 *Phys. Rev.* B **51** 15885
[46] Thomson J R, Hong G, Ryan D H, Zuckermann M J and Grant M 1992 *Phys. Rev.* B **45** 3129
[47] Wohlfarth E P 1978 *J. Magn. Magn. Mater.* **7** 113
[48] Fisher M E, Ma S K and Nickel B G 1972 *Phys. Rev. Lett.* **29** 917